Collagen Denaturation as a Toughening Mechanism in Cortical Bone

by

Corin Alexander Seelemann

A thesis

presented to the University of Waterloo

in fulfillment of the

thesis requirement for the degree of

Master of Applied Science

in

Systems Design Engineering

Waterloo, Ontario, Canada, 2021

Author's Declaration

I hereby declare that I am the sole author of this thesis. This is a true copy of the thesis, including any required final revisions, as accepted by my examiners.

I understand that my thesis may be made electronically available to the public.

Abstract

Bone is a highly versatile tissue. It is used for protecting internal organs as ribs, supporting locomotion as long bone, as a weapon in the form of antler, and many other uses. Depending on its use or function the bone may experience repeated cyclic loads, as in leg bones, or resist sudden impact as antler. To be physiologically useful as a biomaterial, bone must be stiff and resist deformation, but also be capable of dissipating large amounts of energy while resisting failure. All bone meets these biological requirements as a composite of hydroxyapatite mineral, protein (mainly type-I collagen) and water. Together these materials form a highly complex multi-scale structure that gives rise to varied and powerful toughening mechanisms. One putative - but yet unproven - mechanism is the mechanical denaturation (unravelling) of collagen. The native form of collagen is a triple helix with internal hydrogen bonds maintaining the molecular structure. In silico experiments have suggested that collagen does denature under mechanical stresses. If the collagen does mechanically denature during fracture, then some quantity of energy is dissipated disrupting the internal hydrogen bonding. The primary objective of this work is to test the hypothesis that "collagen denatures as a toughening mechanism during stable fracture of cortical bone".

A new biotechnology, fluorescently labelled collagen hybridizing peptides (F-CHP), has seen recent successes in identifying denatured collagen in a variety of tissues. These probes are specific for denatured collagen and not native, triple helical collagen. As such they provide a unique opportunity to probe the behavior of bone collagen during fracture. A notching and staining system was devised to reproducibly image denatured collagen on bovine cortical bone fracture surfaces. This imaging showed consistent increases in staining on surfaces produced by stable crack extension during fracture. This increase in staining correlated strongly with the energy per unit area dissipated by the sample. Furthermore, the staining was confined to a visibly rough region on the fracture surface produced by stable fracture extension. This result supports the hypothesis, suggesting that the denaturation of collagen is a crucial element of how bone resists fracture during stable fracture extension.

Acknowledgements

The author would like to thank Professor Thomas Willett for his excellent supervision and this opportunity to investigate the fundamental behaviors of bone.

The author also thanks his committee members, Professor Stewart McLachlin, and Professor Reem Roufail for reviewing my thesis and providing high quality feedback to improve it.

The author would also like to give special thanks to all his colleagues at the Waterloo Composite Biomaterials Systems lab, and in particular Jindra Tupy, for his excellent advice, and moral support, Daniel Dapaah, for his assistance in preparing samples, and knowledge of fracture mechanics, and Cyrus Fiori for acting as someone to discuss ideas and plans with.

The author would like to acknowledge and thank Dr. Michaela Strüder-Kypke from the University of Guelph for her help in confocal imaging, and for taking confocal images during the COVID-19 pandemic lockdowns when campus access was necessarily restricted.

The author would also like to thank Dr. Dibakar Mondal for his assistance taking SEM images.

Table of Contents

List of Figures

List of Tables

List of Abbreviations

BPC: 'Bright Pixel Count'

BPD: 'Bright Pixel Density'

F-CHP: 'Fluorescently labeled Collagen Hybridizing Peptide

MDPZ: 'Microdamage Process Zone'

MPI: 'Mean Pixel Intensity'

ROI: 'Region of Interest'

SEM: 'Scanning Electron Microscopy'

TEM: 'Transmission Electron Microscopy'

WFx: 'Work to Fracture'

Chapter 1
Introduction: Bone as a Hierarchically Structured Tissue

1.1 Motivation: Toughening mechanisms in bone

Bone as a structural tissue exists in many different forms in many different species, serving multiple roles, such as supporting locomotion, and guarding internal organs. Despite this versatility, its structure features some very consistent motifs [1]–[3]. Consistently, it forms with a nano-structure of collagen protein, arranged in fibrils around hydroxyapatite mineral crystals [1]–[3]. This multi-scale structure of bone enables toughening mechanisms that give it its impressive material properties [4]–[6]. The ability to resist fracture of bone is one such property, on the length scale of <600 microns the fracture toughness (a metric for how difficult it is for a fracture to begin propagating in a material) of human cortical bone is 25 $MPa \cdot m^{1/2}$ and at larger length scales (~1 mm) 2.4-10 $MPa \cdot m^{1/2}$ [7]. Bulk hydroxyapatite has a fracture toughness of 1.2 $MPa \cdot m^{1/2}$ [8]. The ability of bone to resist fracture, particularly on the microscale is far greater than would be expected from its mineral constituent alone. Furthermore cortical bone effectively transfers stresses from the hydroxyapatite mineral crystals to collagen fibrils, supporting strains to failure (a measure of how much a material can deform without breaking) of 1.2% in bovine bone [9]. One particularly important aspect of bone its ability to promote stable fracture, where the energy needed to propagate a fracture through bone increases as the crack extends, this allows for a period of stable crack extension. The ability to resist fracture and demonstrate stable tearing, undergo and undergo strain without failing, are the result of toughening mechanisms that can dissipate energy without while resisting crack propagation during fracture [10], [11]. Toughening mechanisms here are ways in which the components of bone interact with each other to resist fracture, and are enabled by the hierarchical structure of bone [12]. These mechanisms include the formation of a microdamage process zone (MDPZ) within which many small microcracks form around the crack tip, allowing energy to be dissipated away from the main crack, and fibrillar sliding, where collagen fibers are pulled past each other absorbing energy into separating the fibrils plastically [4], [9]. Because the microstructure of bone is anisotropic, the material properties of bone vary based on the direction of applied stresses [13]–[15]. In one experiment it was observed that longitudinally-oriented fracture, where the crack grows along the long axis of the bone, the biomaterial is brittle, but radial or circumferential fracture where the fracture grows perpendicular to the long axis of bone were more ductile requiring more energy to produce fracture [13]. Whether fracture occurs in a brittle or ductile manner is also dependent on the rate of deformation [16]. During

mechanical testing faster deformation is more likely to result in a brittle fracture whereas slower fracture results is more likely to produce a fracture with well-defined stable crack extension [16]. Physiologically this can correspond to strain rates experienced while walking, compared to strain rates experienced during a fall [17]. Bone is toughest at strain rates associated with activities such as walking [16].

Proteins are large biomolecules that naturally form structures (such as helices, and pleated sheets) relevant to their physiological function. When they lose this structure (from oxidative damage, mechanical stress, or thermal effects) it is referred to as denaturation. Mechanically-driven collagen denaturation has been proposed as a toughening mechanism in bone, representing a sacrifice of the structure of collagen molecules to arrest fracture growth [4]. Collagen naturally forms a stable triple helix from three amino acid chains [18]. Separating these chains thermally requires ~70 J/g this is more than double the energy needed to thermally denature most proteins (~20 J/g) [19]. It is a widely accepted idea, even without any experimental data to prove it to date that collagen molecules contribute to fracture resistance in bone through mechanical denaturation. In silico molecular dynamics simulations of a collagen molecule under tensile stress, the internal bonding within the backbone of a collagen triple helix was replaced by hydrogen bonds [20]. Raman spectroscopy investigations of human cortical bone have observed that the quality of the collagen matrix, inferred from the relative intensity of Raman peaks relating to degrees of freedom in which the protein's amides may move, is correlated to the toughness of bone [21], [22]. This implies that that collagen existing in its native state prior to fracture is important to the bone tissue's ability to dissipate energy during fracture. Other research, making use of gamma irradiated bone, has likewise observed that when the collagenous phase of bone is highly damaged, the bone becomes brittle [23]. Thermomechanical analysis of collagen quality in human bone have also shown that markers of poor collagen quality correlate with an inability to dissipate energy during fracture [24]. Furthermore, in soft collagenous tissues mechanical overload produces several indicators of collagen denaturation, such as susceptibility to proteolytic digestion and altered thermal instability [25]–[27]. Presently direct observation of the behavior of collagen on fracture surfaces is missing.

Understanding the underlying properties of bone and how it achieves strength and toughness have been topics of active research for a very long time. This research further explores the question of **how** bone resists fracture at the molecular level.

1.1.1 Hypothesis and objectives

The primary objective of this work is to test the hypothesis that "**bone collagen denatures as a toughening mechanism during the stable fracture of cortical bone**." Additionally, there are further research questions addressed in this work:

1. Is the mechanism of collagen denaturation exclusive to stable crack extension?
2. Can collagen denature as a toughening mechanism during fracture if the bone is dehydrated? The findings of Gautieri's models suggest that water is necessary for this mechanism to occur.
3. How does the quantity of denatured collagen correlate to the energy dissipated during fracture of cortical bone?

These questions help to achieve a more thorough understanding of how this toughening mechanism contributes to the fracture toughness of cortical bone.

Chapter 2
Background and Literature Review.

2.1 Cortical bone microstructure

Cortical bone is the dense compact material that is found in the main shaft of long bones, such as femora and tibiae [28]. It is stiffer, denser (less porous) and has a higher Young's modulus than other types of bone, such as cancellous, spongy bone [28]. In bovine cortical bone, there are two common structural motifs, plexiform and Haversian microstructures [29], [30]. Haversian bone is characterized by osteons forming 100-200 micron diameter cylindrical structures, oriented along the long axis of the bone [1], [4], [28], [30]. The constant remodeling of bone tissue by osteoclasts and osteoblasts results in the formation of osteons. The other common motif is plexiform bone [29], [30]. Plexiform bone is particularly common to large, fast growing animals [1], [31], [32]. Plexiform bone tends to form parallel, interconnected sets of highly mineralized tissue [31]. In general plexiform bone is stiffer than haversian bone [30], [33]. Adult human bone is Haversian [34].

2.1.1 Toughening mechanisms in cortical bone

The multi-scale structure of bone grants it impressive strength and toughness beyond what would be expected of its constituents. The figure below summarizes these toughening mechanisms.

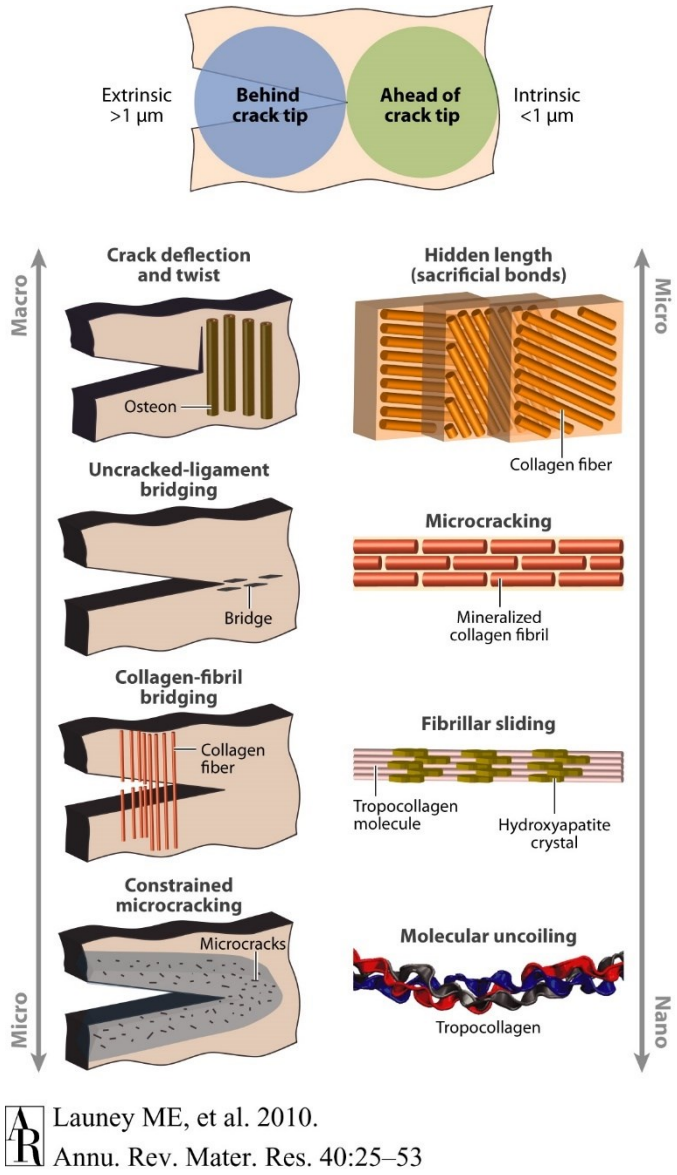

Launey ME, et al. 2010.
Annu. Rev. Mater. Res. 40:25–53

Figure 2-1: Toughening mechanisms in cortical Bone. From Launey et al. 2010. Republished with permission [4].

As shown in Figure 2-1, these mechanisms start with macroscopic behaviors. As a gestalt these toughening mechanisms are how bone prevents a fracture from completely propagating through the tissue. The largest scale toughening mechanism is crack deflection, which is beneficial not only for extending the length over which the crack must grow to completely fracture the bone, but also for changing the direction of crack growth away from the applied stress orientation [4]. The collagen

fibrils bridging the crack support fracture resistance by absorbing energy away from the growing crack front [6]. This is achieved through two ways; first, by partially debonding from the surrounding bone, then through energy intensive fibril 'pullout' where the fiber is separated from one side of the fracture surface [6]. Diffuse micro-cracking as a toughening mechanism has been observed both before a crack begins to grow, and during propagation [11], [35]. The development of these microcracks through bone has been shown to correlated to the post-yield strain in human bones under tensile load; these cracks dissipate energy without creating a singular cohesive crack front. [36]. At even smaller length scales, collagen fibrils can be described as being 'glued' together by cross links, formed from non-collagenous proteins such as osteopontin, and electrostatic interactions (when fibrils are within 10 nm of each other). [37], [38]. The cross links are 'sacrificial' in the sense that they require energy to break and thus completely separate mineralized fibrils, such that the cross link between fibers is sacrificed to resist fracture [37]. These cross links also provide what is described as 'hidden length' in that as mineralized fibrils are pulled apart, it 'reveals' these cross links extending between them and maintaining connection [37].

Interestingly, collagen denaturation is listed as a toughening mechanism in this summary, though the evidence cited for this phenomenon is based exclusively on molecular dynamics simulations [20].

2.1.2 Strain rate dependency in cortical bone

Bone, being a biological tissue, exhibits viscoelastic behavior and as such its material properties depend on applied strain rates [39]. Faster rates of deformation during mechanical testing produce more unstable fractures [16], [17], [40], [41]. In general, higher strain rates (and impact loading) produce unstable, brittle behavior, and slower strain rates produce stable 'ductile-like' behavior in which the bone continues resisting fracture even after the maximum loads are achieved [16], [17], [40], [41]. One factor that can dictate the strain rates needed to produce unstable fracture is age. In a study comparing young bovine bone (6 months old) to mature bovine bone (18 months old), it was observed that for the same strain rate the mature bone behaved in a more unstable manner [42]. In mature bovine bone strain rates of $8x10^{-3} mm \cdot s^{-1}$ consistently causes unstable fracture. In adult human bones the strain rate needed to produce unstable fracture has been observed to decrease with age [16]. In tests on elderly human bone (85 year old donor) strain rates on the order of $10^{-3} mm \cdot s^{-1}$ tend to cause unstable failure, but for young donors (15 years old) the necessary strain rate to consistently provoke unstable crack extension increases to $10^{-2} mm \cdot s^{-1}$ [16]. The exact mechanism that causes this

susceptibility to unstable fracture is unknown, but it is suspected that a loss of collagen quality (potentially through oxidative damage, or caused by disease) plays a major role [16], [24], [43].

2.1.3 Anisotropy of cortical bone

Cortical bone is an anisotropic material, such that its material properties depend on the orientation of the principal material coordinate system relative to the applied stresses. It has often been described as transversely isotropic, with the long axis of bone having different properties than the circumferential or radial directions [30]. More commonly, bone is considered to be orthotropic with the radial, longitudinal and circumferential axis each having its own behavior [14], [15], [44]. The figure below shows these orientations relative to a long bone.

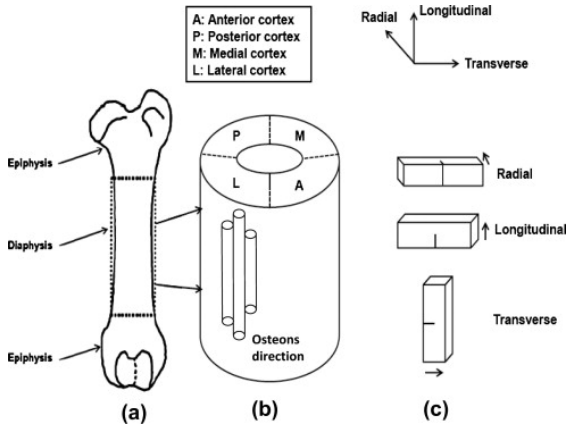

Figure 2-2: Orientation of long bone and crack orientations. From a to c: schematic of bovine femur, position of cortexes in cortical bone, crack orientations in bone. Reprinted from Li et al. 2013 with permission [45].

Radial fracture is oriented from outside the bone to the center of the bone and tends to be heavily deflected by osteon cement lines. Transverse fracture runs across collagen fibrils, which will typically be pulled out of the fracture surface as a toughening mechanism. Longitudinal fracture breaks between cement lines, minimizing deflection [46]. Because these orientations dictate how the fracture will grow through bone, they play a large role in the fracture mechanics. Fractures that grow longitudinally generally require less energy to grow than in the other orientations [46]. When the crack growth is well aligned with collagen fibrils in bovine tibia and femur bone, the energy to extend a crack is 0.375mJ/mm^2 and when the fracture is perpendicular to the fibrils is 9.92 mJ/mm^2 [13].

Longitudinal fractures also tend to both deflect less than radial and transverse fracture and be more brittle [13].

2.1.4 Dependence of mechanical properties of cortical bone on storage media

Prior work simulating the behavior of collagen under load has predicted that, when overstressed mechanically, collagen molecules denature, forming hydrogen bonds with water [20]. When not kept hydrated, the mechanical properties of bone can change [22]. The largest impact is on work to fracture (WFx) which has been observed to decrease to 43% of its hydrated value during transverse fracture of bovine tibia [47]. Bone stored frozen maintains its mechanical properties provided it is rehydrated before any testing [48]. When stored in ethanol, rather than saline bovine bone becomes much more brittle and exhibits minimal stable behavior [47].

2.2 Application of fracture mechanics to bone

The study of fracture mechanics seeks to understand under what circumstances can a crack or fracture grow through a material [49]. Fracture mechanics approaches consider local behavior around defects, such as voids or cracks, and under what conditions these defects lead to failure [49]. Two commonly reported metrics are critical stress intensity factor (Kc), and the J-integral (also called nonlinear energy release rate) [49], [50].

2.2.1 Critical stress intensity factor Kc

Defects in materials exist as stress concentrators. What this means is that is some stress applied remotely to the defect location, also called far-field stress (σ_{inf}), applied to a large material that contains a defect (such as a void or a crack) then the region close to this defect will functionally experience a stress greater than σ_{inf}. As an example, for an infinite plate with an ellipse shaped defect the following equation calculates the maximum tensile stress intensity experienced at the defect [49]:

$$\sigma = \sigma_{inf} * (1 + 2\sqrt{\frac{a}{\rho}}) \quad (1)$$

Here σ_{inf} is the far-field stress and σ is the stress experienced at the defect. a is the long radius of the ellipse and ρ is the radius of curvature $\rho = \frac{b^2}{a}$. This is illustrated in the figure below.

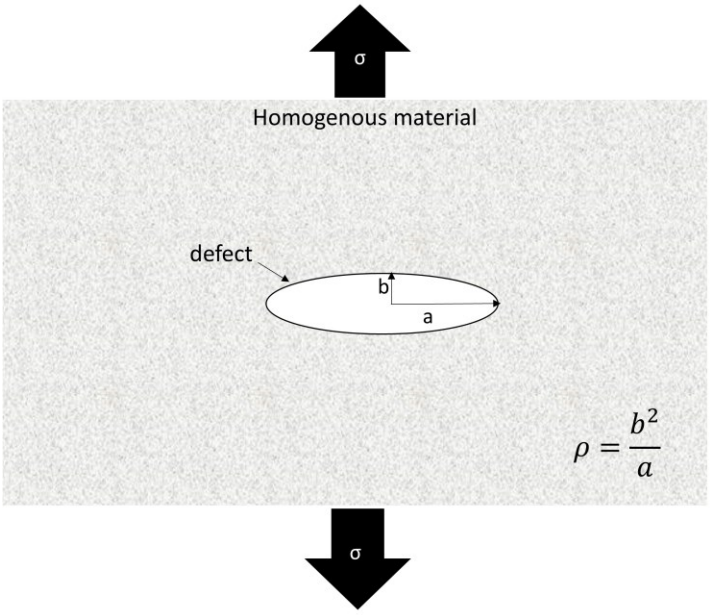

Figure 2-3: Illustration of an elliptical defect in a material.

A notable implication of this is that even very thin cracks can have a substantial impact on the stresses experienced by a material in the vicinity of a defect; potentially causing the material to fail under loading it might withstand in the absence of a defect [49].

A stress intensity factor (K) can be calculated that evaluates the impact a defect has on a material [49]. Critical stress intensity or fracture toughness (Kc) is the stress intensity (also called 'fracture toughness') that results in crack propagation through a material [49], [50]. Determining Kc requires measuring the force needed to induce crack growth around a defect with a known geometry. One method that has been successfully used to measure Kc, both in bone, and other brittle materials, is chevron notched bending tests [51]–[53]. The equation below shows the calculation from ASTM C1421-18 for fracture toughness in a chevron notched geometry under four point bending [51].

$$Kc = Y^*_{min} * \left(\frac{P_{max}{}^*(S_0\text{-}S_i)}{BW^{\frac{3}{2}}}\right) \quad (2)$$

Here Y is a geometric coefficient based on the notch geometry, P_{max} is the maximum force applied before the crack began to propagate, S_0 -S_1 is the difference between outer and inner loading spans, B

is the length of the dimension perpendicular to crack growth, W is the length of the dimension in line with crack growth. This Kc value is a material property, describing that if within a material a stress intensity greater or equal to Kc exists then a crack will propagate through the material. Previous research has shown that the Kc of bovine femur can be measured and calculated with multiple methods (single edge notched, compact tension, chevron notched) and generate consistent results within a range of 2.4-6 $MPa \cdot m^{1/2}$ [52].

2.2.2 J-Integrals

Fracture toughness corresponds to the stress needed to grow a crack in a material, comparatively the J-int measure can be used to evaluate the energy needed to extend a crack. The J-integral itself is a contour integral, that when the contour contains the crack tip, is equal to the energy release rate G in linear elastic fracture mechanics [49]. One particularly common use for G or J is plotting the R curve, which shows the energy needed extend a crack, as the crack grows [49]. Bone is described as demonstrating rising R-curve behavior, where the energy needed to extend a crack increases as the crack grows, until unstable fracture occurs [11], [50], [54].

2.3 Work to fracture of cortical bone

Work to fracture (WFx) is the total amount of work done to completely fracture a sample mechanically. It is calculated by taking the entire amount of work done on a sample during a mechanical test that results in fracture and dividing by the area of the fracture surface. WFx is sometimes calculated dividing by twice the area of the chevron notch [40], [47], [55]. Dividing the total work by just the area is not uncommon [16], [23], [56]. In this thesis when discussing WFx from prior research the units were converted to mJ/mm^2 and if the WFx was calculated by dividing by twice the fracture surface area the value was multiplied by two for comparison. WFx does not account for the specimen geometry unlike methods of determining fracture toughness like Kc, G or the J-integral. Modifying the test geometry will influence the results. Chevron notched bovine femur fractured at very low rates ($8 \cdot 10^{-4}$mm/s) have been reported as having a WFx value of 2.4-6.6 mJ/mm^2 [40]. A four-point bending test using a single edge notch with a razor used to create a pre-crack performed on bovine femur had 7.1±1.4 mJ/mm^2 as the WFx [56]. In single edge notched bovine bone under three point bending, a WFx of 12.8 ±4.4 mJ/mm^2 was reported [23].

2.4 Fluorescently labelled collagen hybridizing peptides

Fluorescently-labelled collagen hybridizing peptides (F-CHP) are a relatively new biotechnology with tremendous use in differentiating collagen in its native state from denatured collagen. The structure of these peptides mimics the primary structure of collagen α-chains, containing glycine-proline-hydroxyproline repeats [57]. This probe, by mimicking collagen, can hydrogen bond to denatured collagen strands in the same manner that intact collagen self hybridizes forming the triple helix [57]. The collagen needs to be denatured for this staining to occur, otherwise there is no site where F-CHP can favorably bind. This is illustrated in the figure below from Zitnay et al. 2017 [58].

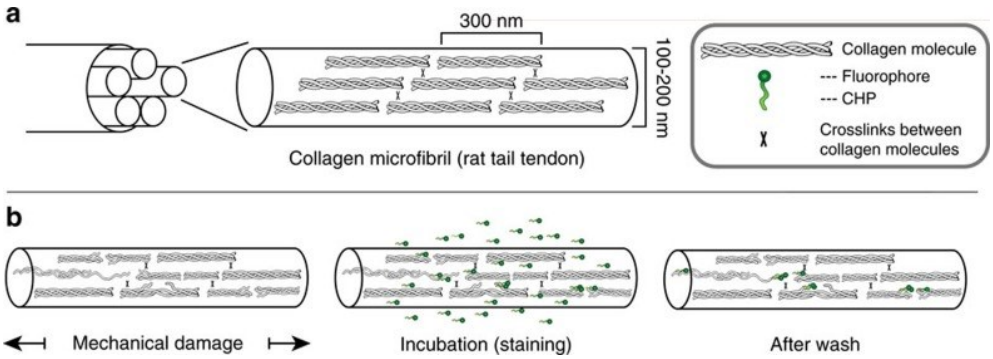

Figure 2-4: Schematic of how F-CHP binds to rat tail tendon collagen. CC-BY 4.0 from Zitnay et al. 2017 [58].

In determining the efficacy of these probes, the CHP group has been complexed to both fluorescent dyes for fluorescent imaging and to gold nanoparticles [57]. To produce damage, detergents, such as SDS, were applied to Porcine tissues and compared to tissue that was not exposed to any detergent [57]. Below is a figure from Hwang et al. 2017 showing how F-CHP staining increases on porcine ligament as the concentration of SDS detergent it was incubated in increases. In this figure, "CF-SSCP" is a control which is F-CHP with the amino acid sequence of the probe is scrambled, such that it should not have affinity for denatured collagen.

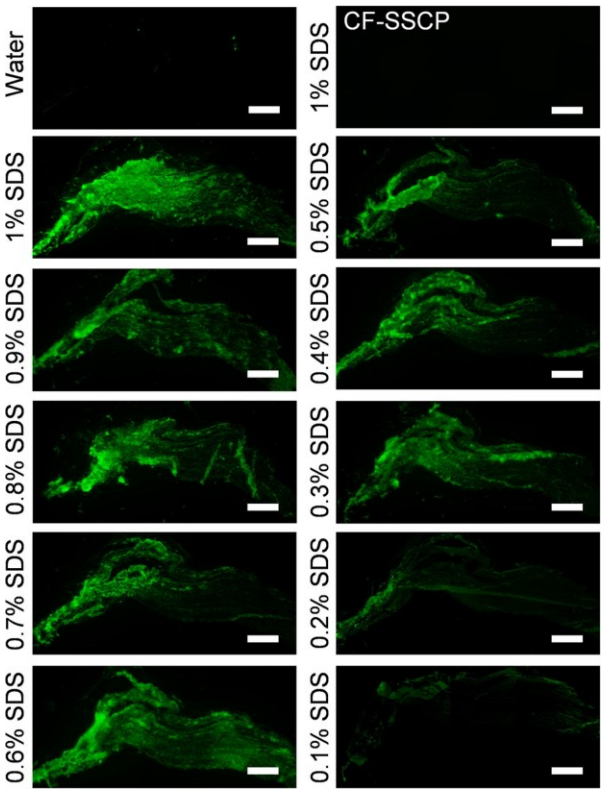

Figure 2-5: Collagen denaturation on porcine ligament due to SDS treatment results in greater staining with F-CHP. Scale bars are 1 mm. CC-BY 4.0. Figure from Hwang et al. 2017 [57].

As an additional corroboration of this method, the probes were complexed to gold nanoparticles, which allows imagining via transmission electron microscope, shown below [57]. In this figure, SDS, CHAPS, SD, and Triton X-100 are all detergents and surfactants used on the tissue to induce denaturation. Red dots are where the gold nanoparticles on the bound CHPs produced signal [57].

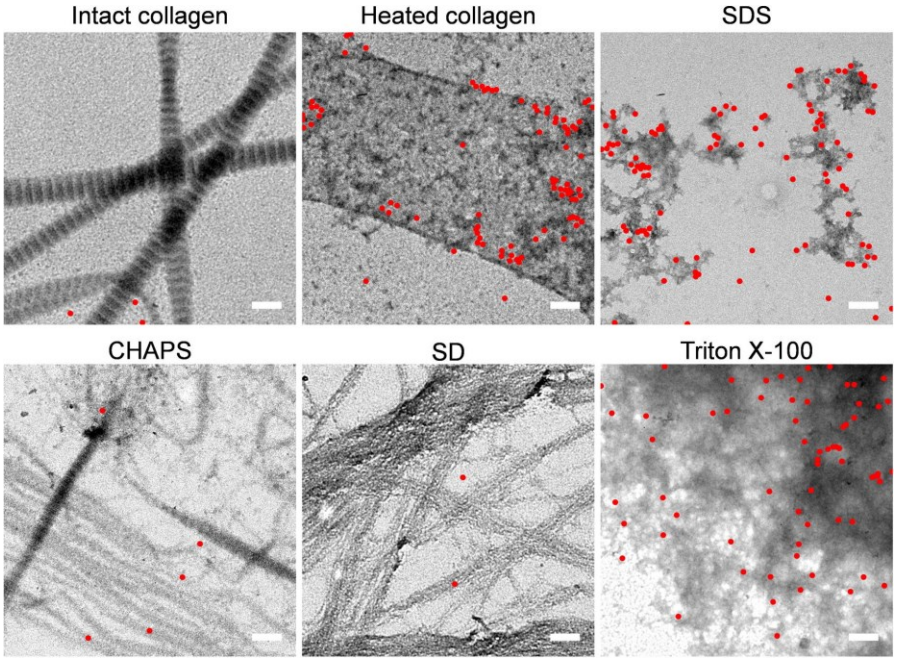

Figure 2-6: TEM image of CHP bound to denatured collagen. Scale bars are 500 nm. CC-BY 4.0. From Hwang et al. 2017 [57].

The paper by Hwang et al. cited previously is foundational to demonstrating the functionality of F-CHP as a specific probe for denatured collagen. This has been further used in a variety of contexts to identify the denaturation of collagen in tissues. In sheep cerebral arteries, F-CHP was used to identify damage resulting from overstretch, which was detected using confocal microscopy [59]. In the images of sheep arteries, a threshold was based off of unstretched tissue to identify a level of staining that indicated damage caused by overstretch [59]. This damage was localized to fibers that were aligned with the loading direction [59]. Rat tail tendons subjected to high tensile loads, or cyclic tensile loading also stain highly with F-CHP [58], [60]. Here the mean fluorescence of the stained tendons was used to evaluate the change in the collagen state compared to undamaged tendon [58], [60]. The change in collagen signal was compared to a change in susceptibility to trypsin digestion [58], [60]. Trypsin is a proteolytic enzyme that preferable digests denatured collagen rather than triple helical collagen [27]. F-CHP has also been used to observe that, as intervertebral discs degenerate with age, the collagen within them progressively becomes less likely to be found in its native, triple helical state, but rather in a disordered/denatured state [61]. Overall, F-CHP has been used to successfully

image denatured collagen in a variety of contexts providing novel data regarding the molecular level state of collagen.

Chapter 3
Materials and Methods

3.1 Beam preparation

Mature bovine bone was acquired from a local butcher as whole tibia. Bovine bone was selected for most experiments described in this section, as it is easy to acquire for research use. The steers were mature (18-24 months old) at time of slaughter. These bones were stored frozen to prevent any decay until further work was done. To begin the process of preparing beams, they were thawed and cleaned of any soft tissue and refrozen. Then they were cut using a 14-inch band saw (Craftex CX104, Busy Bee Tools, Concord, ON) to remove the ends of the bone where they were connected to joints, and then cut along the long axis of the bone to separate the posterior and anterior cortex sections. These sections were frozen until further work was done. Freeze thaw cycles were intentionally kept to a minimum to prevent temperature changes from impacting the properties of the bone. In general cortical bone has been observed to have no discernable changes in mechanical properties with <5 freeze thaw cycles [62]. The figure below shows the relatively flat section of posterior cortex used in this work.

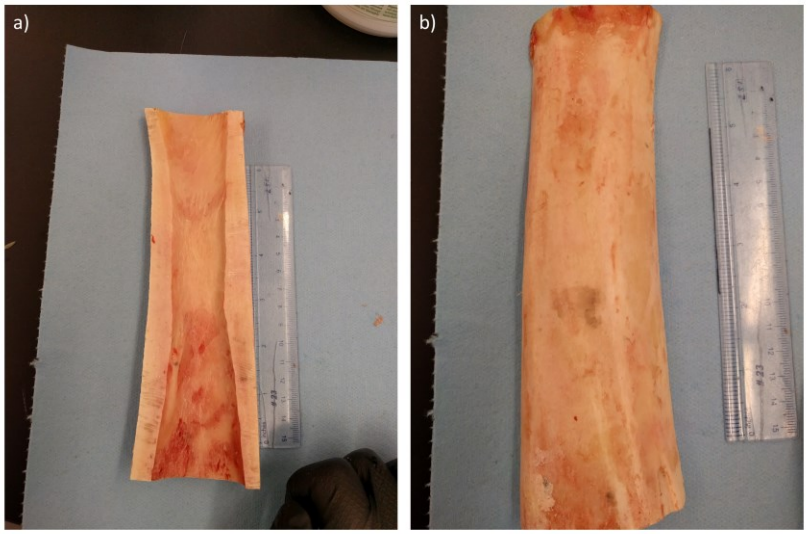

Figure 3-1: Bovine tibia a) Endosteal cortex. b) Periosteal cortex.

This section of bovine tibia was selected because it is large enough to cut ~6 bone beams for mechanical testing. Since these beams all come from nearby to each other, they are expected to behave similar to each other during mechanical testing and to have similar biochemistry.

Two bovine tibiae posteriors from the same steer were milled to 4x4x50 mm^3 beams, with their long axis aligned parallel to the long axis of the bone. To achieve this the bones were first cut abrasively with a diamond blade using a pathology bandsaw (IMEB, San Marcos, CA) to isolate a large flat 'plateau' of cortical bone, removing the curved regions shown above. This was then milled with a CNC vertical mill (CNC mini mill, Sherline products, Vista, CA) into a long (~110 mm) flat section from which the beams could be cut out. While the bone was being milled, a shop vacuum with a HEPA filter was continuously run to remove dust produced by the milling process. The flattened bone was then cut in half with the pathology band saw. Finally, the beams were cut with using an ISOMET low speed metallurgical saw (Buehler, Lake Bluff, IL).

Six beams were milled from each posterior section, for a total of twelve beams. The anterior section was not used in this work. The bovine beams were labelled with a two number code such as '1-1'. The first number was 1 or 2 and indicated the source bone, the second number was 1 to 6 and was arbitrarily assigned. Beams with an odd second digit were used in the dehydrated tests (i.e., 1-1, 2-5) and beams with an even second digit (i.e., 1-4, 2-4) were used in the hydrated tests.

These beams were then chevron notched with a custom-made stainless steel cutting jig. A schematic for this jig is shown in Figure 3-2. This jig was based off of prior work (Jenkins et al. 1988) designing cutting tools for creating chevron notches in ceramic materials with a circular cutting tool [63].

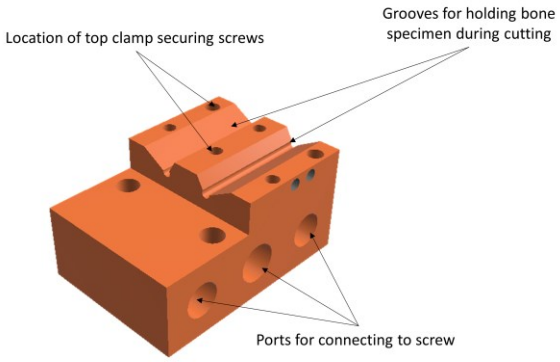

Figure 3-2: Schematic of the chevron notching jig.

The figure below shows several perspectives on the chevron notching jig.

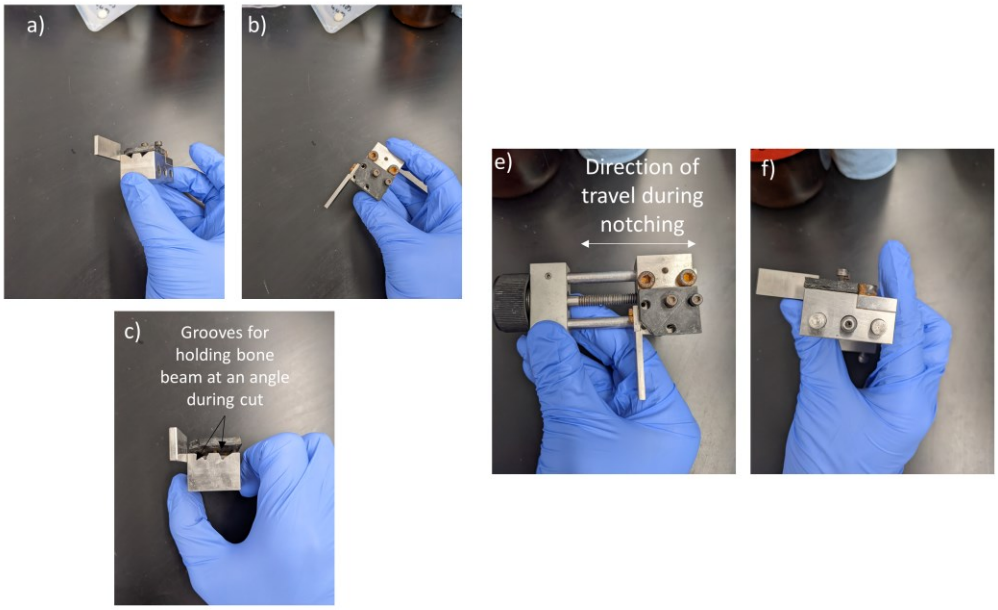

Figure 3-3: Cutting jig perspective photos. a, b, c) Show the chevron notching jig with the plastic top clamp (black) attached. e, f) Show the jig with the attached screw that allows for controlled travel of the jig for cutting.

While in operation, the bone beam is placed into one of the top grooves and held in place by plastic clamp. A ‘backboard’ is screwed into the device such that the bone has the same amount of room in both channels. To get a proper notch, the bone is cut first in one groove then rotated 90º and placed in the other. A picture of the device in operation is presented in the figure below.

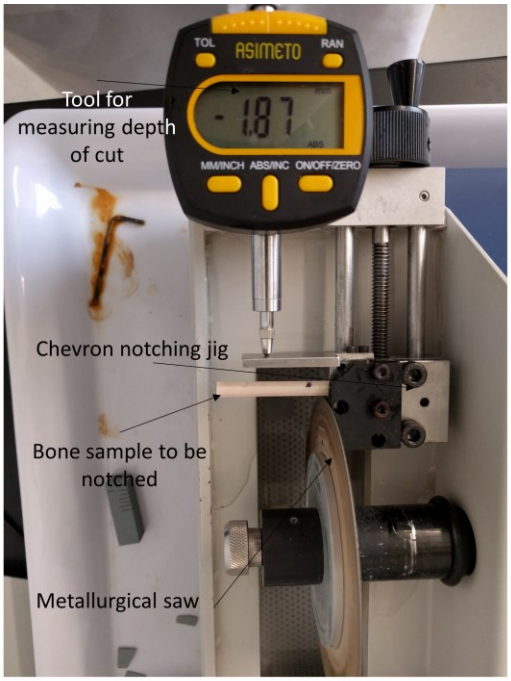

Figure 3-4: Top-down view of cutting jig in operation on the metallurgical saw. During cutting the bone sample is moved by the jig into the saw.

This cutting produces a chevron notch with a 60º notch angle in the triangular ligament with a width of 0.3 mm. This notching setup was based on ASTM C1421-18. However to comply fully, the beam would need to have a 4 mm by 3 mm area cross section [51]. For ease of accurate and consistent notching a 4 mm by 4 mm area cross section was used, ultimately making the notches non-compliant for the purpose of calculating the fracture toughness. Even with this limitation chevron notches provide substantial benefit in this work. A key advantage of the chevron here is that it promotes stable crack extension as the crack front expands as the fracture travels through the triangular ligament [41], [52], [53], [63]. A second advantage is that chevron notches are good for producing very pure mode I (opening) stresses during fracture, minimizing deflections and possible shear or transverse loading [51]. Chevron notches also self precrack, removing the need for manually adding a starter crack to the

specimens [52]. The tip of the triangular ligament faced the circumferential transverse direction as it is referred to in Figure 2-2 [46]. This direction of loading is expected to deflect cracks less strongly than radial loading, but still allow collagen fibrils to participate in crack resistance [13], [45]. Large crack deflections would be an obstacle to sample imaging as confocal microscopy has a limited depth of field.

3.2 Beam fracture

For the hydrated group, the beams were placed in 15 ml centrifuge tubes filled with 1M PBS with 50 mM CaCl to rehydrate overnight (19 hours). This was intended to be adequate to fully rehydrate the bone beams. In past work, a minimum time of 4 hours has been needed to fully hydrate bovine bone beams for fracture testing [11]. Dehydrated beams instead were air dried overnight (20 hours) in a sealed desiccator with the atmosphere removed via vacuum. In human beams, a reduction in stable behavior and WFx can be observed after 4 hours of air drying at room temperature [64].

All beams were placed in a four-point bending configuration and fractured with a crosshead displacement rate of 4 microns per second. ASTM C1421-18 suggests either 3-point or 4-point bending for chevron notched geometries [51]. 4-point bending was selected for this work as it avoids shear stresses between the loading span supports [65]. This loading rate was very slow to avoid any ductile to brittle transition as a result of deformation rate [16], [40]. The support span was 40 mm, and the loading span was 18 mm. The notch was set to face the support span such that the tip of the ligament experienced tensile stress from bending. This arrangement is shown in the figure below.

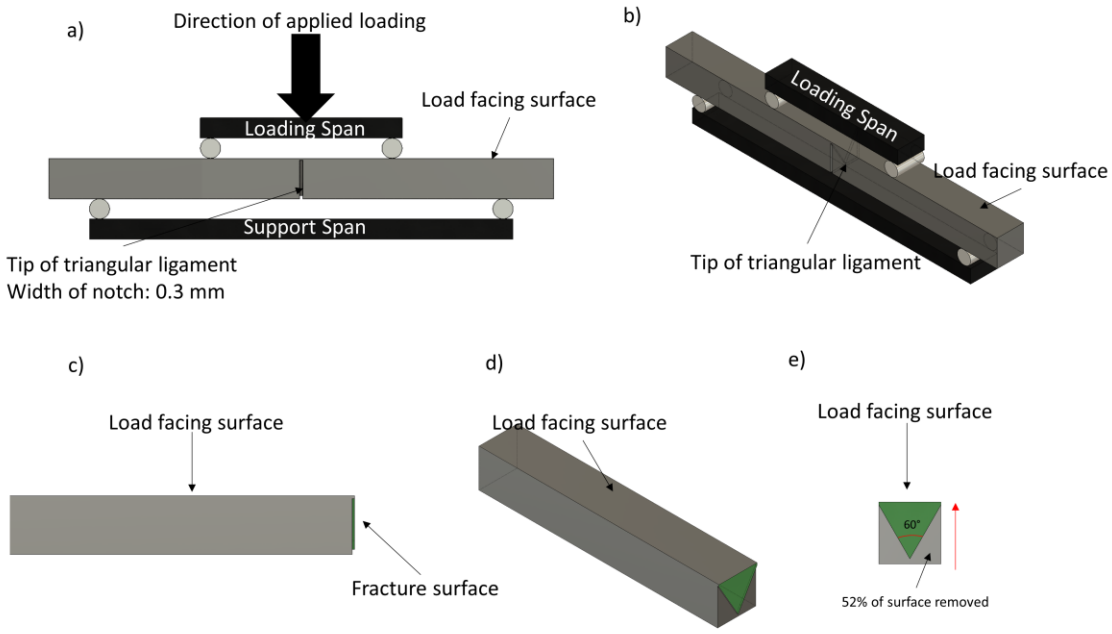

Figure 3-5: Beam bending schematic. a) Beam bending schematic. a) Side view of beam being loaded. b) Isometric view of the beam being loaded. c) Side of view of the beam after fracture in the orientation of a). d) Isometric view of the beam after fracture, in the same orientation as b). e) Head on view of the fracture surface. Red arrow indicates direction of fracture growth on the triangular ligament. The fracture surfaces in figures c, d, and e are highlighted in green to distinguish them from surrounding bone (gray).

Force and deflection were recorded with a sampling rate of 20 Hz during the test. After fracturing under 4-point bending, the samples were prepared for imaging using laser scanning confocal microscopy (Section 3.3).

3.2.1 Load displacement curve analysis

The primary measurement used to assess the behavior of bone in this study was work to fracture applied to the sample (WFx). This was calculated by numerically integrating the area under the curve of the load-deflection curve in Excel using the trapezoidal rule and dividing by the total area of the fracture surface. Based on ASTM C1421-18, the specimen was judged to have undergone some period of stable crack extension if the sample continued to resist fracture after reaching the maximum load [37]. On a load-deflection curve, this appears as the load decreasing while deflection continues.

The area of one fracture surface from each beam was measured optically, by using a pen microscope to take an image of the surface with a known scale bar visible and then tracing the visible notch in ImageJ to compute the area.

3.3 Staining and specimen prep for confocal microscopy imaging

To prepare for microscopy, the fracture surfaces were cut from the broken bone beams along with ~1mm of bone from behind the fracture surface using a metallurgical saw. From each beam, a 1mm section and a 3mm section were cut out from further behind the fracture surface to use as unloaded controls. The 3mm section was polished using graduated polishing trays from 45-micron grit with deionized water to 0.05-micron grit with diamond suspension. In prior research, polishing has been used to expose bone microstructure for microscopy-based analysis [66], [67]. After polishing, only a ~1 mm thick section would be left. The polished surface represents the 'native' behavior of the bone tissue in this test, without any signal produced by sectioning with the metallurgical saw. The surface that was not polished gives an expected level of staining produced by cutting with the metallurgical saw. When the fracture surfaces are imaged, the area surrounding the fracture surface can be seen. This region is produced via metallurgical saw cutting during notching, so it should behave similarly to an unpolished control.

One fracture surface and both cut sections from each mechanical testing beam were partially demineralized overnight (24 hours for hydrated group, 19 hours for the dehydrated group), in 0.5M EDTA solution. This time was sufficient to produce visible change in the texture of the bone surfaces, indicative of the removal of mineral present. The pH of the EDTA solution was increased to ~7.4 using sodium hydroxide, to prevent the acidity of EDTA from impacting the experiment. The demineralization was performed to ensure that the hydroxyapatite mineral could not interfere with staining, either by acting as a source of hydrophilic sites for F-CHP adsorption, or as a spatial hindrance interfering with F-CHPs ability to diffuse. EDTA is a chelating agent that selectively binds to metal ions such as Ca^{+2} forming water soluble complexes [68]. EDTA was selected as a demineralizing agent as it has been successfully used in the past to expose demineralize bone without disrupting the collagen [43], [69]–[71]. After this partial demineralization, the samples were stained in a 96-well microplate, with 100μL of 10μM F-CHP (3Helix Inc, Salt Lake City, UT). F-CHP, like collagen, can self-hybridize, so to 'activate' it, the probe strands must be thermally separated [72]. This was achieved by placing the 5ml centrifuge tube containing the staining solution in a water bath

that had been raised to 80ºC on a hot plate for 15 minutes and then quenching it for one minute in room temperature, in accordance with published methods [57]–[59], [72]. The quenching is necessary to ensure that the staining solution does not induce thermal denaturation of the sample being stained. The dead time between heating and staining was approximately three minutes. The rehybridization half-life of F-CHP is ~3 hours, so they will not have adequate time to self-hybridize during quenching [72]. The samples were allowed to stain overnight (25 hours for dehydrated group, 18 hours for hydrated group) at 4ºC. With the self-hybridizing half-life of 3 hours the expected amount of F-CHP available after 18 hours for staining would be ~2% of the original quantity if no binding to the sample occurred [72]. In prior work (Hwang et al. 2017) >16 hours staining has been used to ensure adequate time for F-CHP binding [73]. After staining each sample was washed five times in ~1 ml of DI water to remove any adsorbed material. The samples were then placed on glass slides under a glass coverslip which held them in place during transport and imaging.

3.4 Confocal microscopy

The stained surfaces (fracture surfaces, controls) were imaged using a Leica TSC SP5 scanning confocal microscope (Lieca Microsystems, Concord ON) located at the University of Guelph's Advanced Analysis Center. The fluorescent probe on the F-CHP is a Fluorescein derivative (5-FAM) with its excitation peak at 494 nm and its emission peak at 512 nm [72]. The excitation light used for confocal microscopy was a 488 nm argon laser at 15% power, and the emission filter used the built-in settings for Fluorescein isothiocyanate (FITC) signal isolation with a window of 500-535 nm wavelengths being permitted to reach the detector. The 488 nm excitation laser was chosen over the 496 nm laser to ensure that the excitation light could not 'bleed through' and appear in the image. 488 nm light is sufficiently close to the 494 nm emission peak to excite F-CHP and has been used successfully to do so in prior research (Hwang et al. 2017, Converse et al. 2018) [57], [59]. FITC and 5-FAM are very closely related molecules, so the built-in filter settings were suitable for easily producing a clear and well-resolved fluorescent image. The laser power was chosen such that the stained surfaces would be clearly visible.

The objective lens had 10x magnification, allowing for each image to be ~1.5 mm x 1.5 mm while maintaining a resolution of 1024 x1024 pixels giving ~1.15 μm x 1.15 μm per pixel. The level of magnification allowed the fracture initiation site to be in the context of the area further behind the fracture. All samples were imaged as Z-stacks with the stack size chosen to obtain a 3D image of the

entire depth in which signal was visible. Fracture surfaces were taken with an additional tile scan to image both the region of fracture initiation but also further behind the origin of fracture on the notch.

Fluorescent imagining of hydrated and dehydrated sample groups were performed separately but under the same microscopy conditions, except that the gain in the dehydrated sample set was slightly (<1%) higher, by accident. Given the small discrepancy no image adjustment was made.

3.5 Image analysis

All raw image data was accessed and analyzed with the FIJI release of ImageJ [74].

3.5.1 Analysis of F-CHP stained control surfaces

The polished and unpolished sections were used as 'negative' and 'positive' controls, respectively, to identify the impact of damage on staining. Each sample was imaged as a Z-stack. A Z-stack is a set of images each taken at a different vertical position to produce a 3D scan. Here, each scan was 9.9μm apart, intended to be close to the ~10 μm depth of field, such that there would be minimal overlap between images. These stacks were projected to a 2D composite image using the "Z project" function in ImageJ with the function "max intensity". The mean pixel intensity (MPI) was then calculated for the entire image. The polished controls were then used to define a threshold value to identify 'damaged' collagen. Each image was thresholded using ImageJ's "threshold" function in the "analyze" menu. Thresholding an image effectively makes the image binary, such that each pixel has a value of 1 (white) or 0 (black). Prior to thresholding, each pixel has an intensity value from 0-255. The threshold that had 99.95% of pixels below it was tabulated for each polished control. A pixel that is brighter than that threshold level contains denatured collagen that must be a result of damage. The threshold of 99.95% was intended to ensure during fracture surface analysis that background levels of staining were correctly rejected (below the threshold). For both the hydrated and dehydrated beam sets, the median threshold was computed for use in subsequent analysis. The dehydrated and hydrated beams were compared to each other in one analysis. For this analysis the higher median threshold was applied to ensure that both comparisons had a consistent limit for isolating signal specific to damage and prioritize excluding background noise.

3.5.2 Fracture surface analysis

The fracture surfaces were analyzed based on the threshold value from the polished controls to identify staining attributable to damage from the fracture of cortical bone. Two techniques were used

to measure the damage: ‘Bright Pixel Density’ (BPD) and ‘Bright Pixel Count’ (BPC). The hydrated fracture surfaces had clearly defined ‘rough’ regions, these were used as regions of interest (ROI)s. The area of these ROIs was measured by tracing them in ImageJ and using the ‘measure’ function to calculate the traced area. Pixels in these images have a known area of 1.15 μm x 1.15 μm. BPD refers to the density of pixels within this ROI and is presented an area percentage. Dehydrated samples did not have a distinct rough ROI, so the area used to calculate BPD was the entirety of the visible fracture surface. BPC is the total number of pixels above the applied threshold on the fracture surface. This count is done without projecting the image to a single 2D composite image as was done with the control surfaces. This allows a 3D view of the staining behavior. This includes any signal above threshold outside of the aforementioned ROI. The dehydrated samples had considerable variance in the amount of fracture surface visible, so only BPD was used. BPC would be biased in these cases to underestimate the staining in samples with less visible fracture surface. The hydrated samples had less variance in imaging.

BPC was intended as a constrained method because it did not make use of the presence of an ROI to inform its output. The BPD method requires the author to select an ROI within the fracture surface according to their best judgment and the exact placement of that ROI impacts the results. BPC only requires identification of the fracture surface. The two methods should correlate with each other, but if there was a high disagreement between them that might indicate that the ROI used for BPD was inappropriate or poorly chosen.

3.6 Statistical analysis for hydrated and dehydrated samples

For all statistical tests, significance was taken at the $\alpha \leq 0.05$ level. It was assumed for the purposes of analysis that the data present follows a normal distribution.

3.6.1 Statistical analysis of mechanical behavior

The means of the mechanical characteristics (WFx, max load, max displacement) of each group (hydrated, dehydrated) were compared. A two tailed student’s t-test was used to determine if the means were significantly different. Prior to the t-test, an F-test for variances was performed to determine if the difference in variances between hydrated and dehydrated samples for each aspect was statistically significant. If it was, a heteroscedastic t-test was used, otherwise homoscedastic t-test.

The impact of notching variance was also assessed. The relationship between notch area and WFx, max load, and max displacement was calculated using linear regression in Excel. The statistical significance of the correlation coefficient was determined based on a two-tailed student's t-distribution.

3.6.2 Statistical analysis of fluorescent behavior

MPI of all controls were calculated. The significance of the difference in mean MPI between polished and unpolished samples was determined by a paired two tailed t-test. Each polished control was paired to the unpolished control from the same beam.

The correlation between WFx and BPC and BPD was calculated for the hydrated samples The significance of the correlation coefficient was determined based on a two-tailed student's t-distribution. The correlation between WFx and BPC was also calculated for the dehydrated samples with significance determined from a two-tailed student's t-distribution.

3.7 SEM-confocal comparison

One additional bovine cortical bone beam was prepared from a separate posterior tibia and used to generate a comparison between SEM analysis and confocal microscopy analysis. This bone beam was not included in analysis described previously as it came from a separate steer. The surface analyzed under confocal microscopy was prepared alongside controls as described in sections 3.3 to 3.5.1, except that it was frozen after fracture and before staining, unlike all other samples. The surface analyzed under SEM was not demineralized or stained. The SEM imagining was done with a Quanta FEG 250 (FEI, Hillsboro, OR) in the WATLAB at the University of Waterloo using environmental mode (low vacuum) and a 20Kv accelerating voltage.

3.8 Human bone preparation

Two human bone beams were prepared separately from the bovine bone beams. These beams were prepared from the medial femur diaphysis of one 21-year-old donor. Since only two beams were prepared, these were labelled as being the proximal or distal beam, based on location taken from the femur. Both beams were notched, stained, and imaged as described in section 3.2-3.4, with the exception of being frozen at -80ºC rather than -20ºC. -80ºC freezer space is limited so human bones

are prioritized for it over bovine bones. The bone source was Regenerative Medicine, Thunder Bay, Ontario. Ethics approval was received from University of Waterloo Research Ethics Board.

Chapter 4
Results and Analysis

4.1 Mechanical behavior of bovine bone

Mechanical data was recorded in the form of load-deflection curves. The figure below shows the curves for all hydrated bovine specimens. The number labels were assigned to allow for cross referencing of samples and associated images.

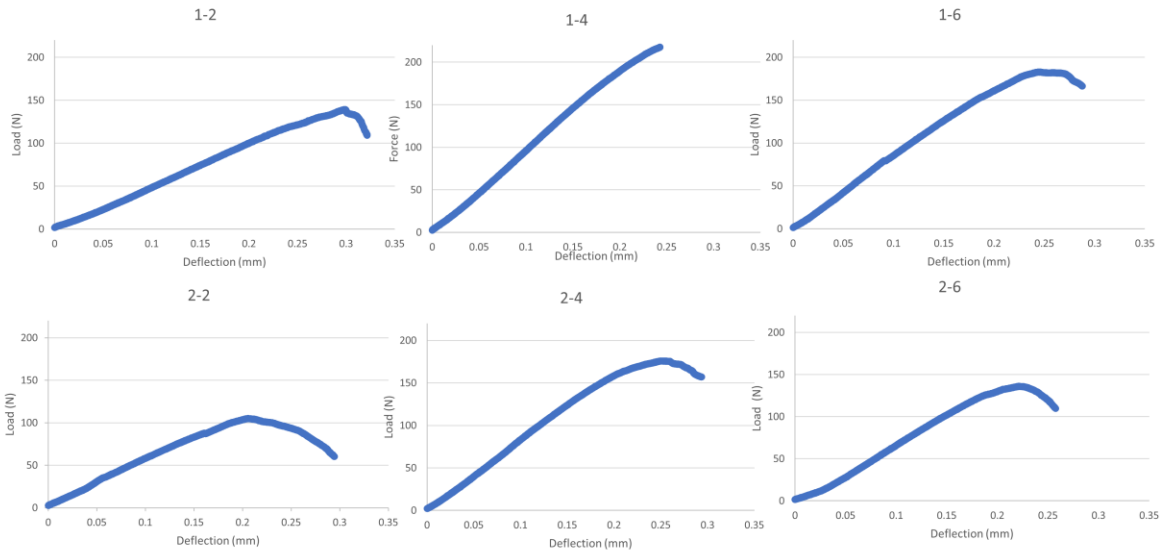

Figure 4-1: Load deflection curve for all hydrated samples.

Sample 1-4 from this set was notable for fracturing in an unstable manner, with no deflection after reaching peak load. All other samples had some extent of stable behavior. The mean WFx of these samples, was 4.63±0.81 mJ/mm^2. It is not uncommon for bovine bone to occasionally fracture in an unstable manner, even with test conditions that promote stable fracture (hydration, chevron notching, slow deflection rates) [52]. As such, the unstable behavior of sample 1-4 is likely a natural outcome of using bovine bone.

The dehydrated bovine samples displayed highly brittle behavior. The load-deflection curves for those specimens are shown in Figure 4-2.

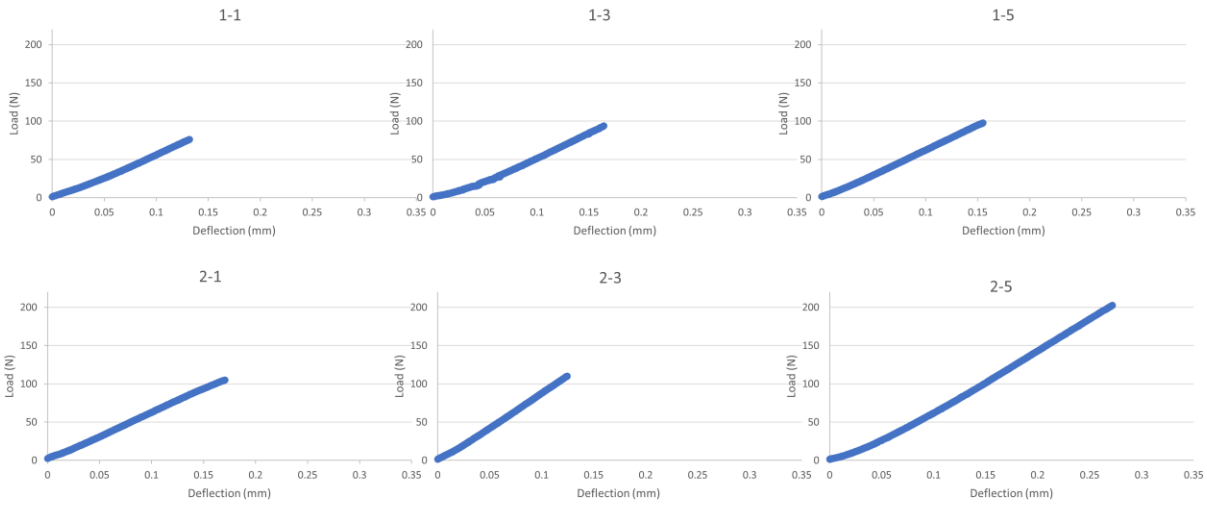

Figure 4-2: Dehydrated fracture surface load deflection curves.

All dehydrated samples displayed linear behavior and unstable fracture. Sample 2-5 was excluded from all further analysis, as it deflected outside of the cut notch. The mean WFx of these samples was 1.34±0.47 mJ/mm^2. Dehydrating the samples had the intended impact of compromising the ability of the samples to undergo stable crack extension.

4.1.1 Comparison between the mechanical behaviors of hydrated and dehydrated bone beams

The mean max load, max displacement and WFx were compared between dehydrated and hydrated bone beams. Figure 4-3 to Figure 4-5 show this data.

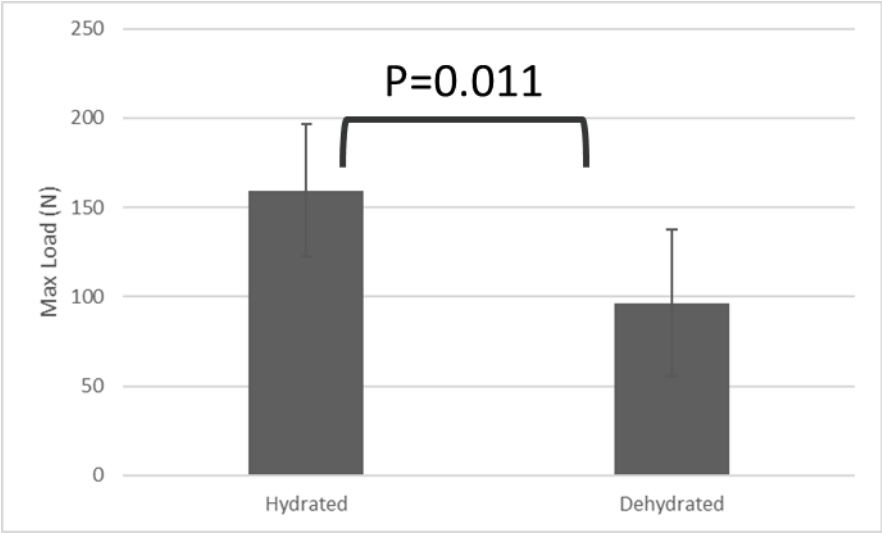

Figure 4-3: Comparison between mean max load in hydrated and dehydrated bone beams. Difference in means significant at P<0.05 based on heteroscedastic two tailed t-test. Error bars are ±1 standard deviation.

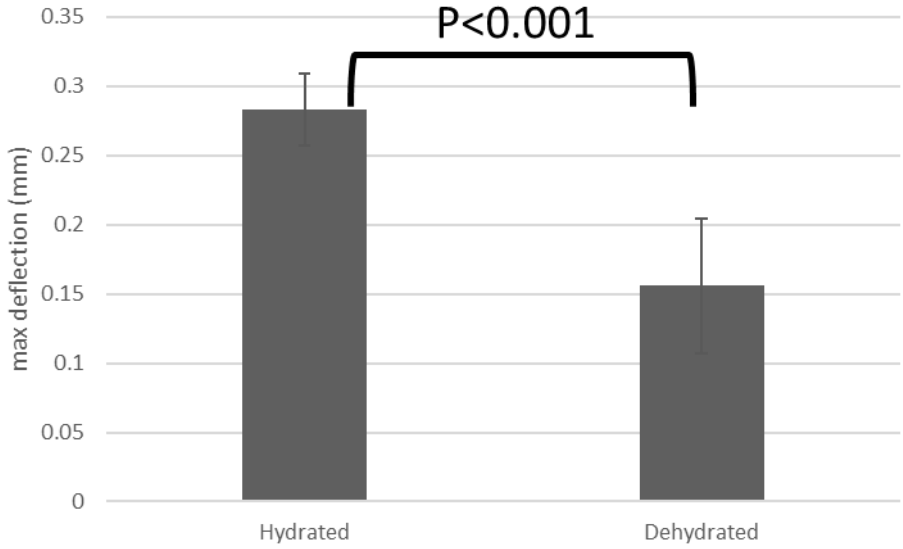

Figure 4-4: Comparison between mean max deflection in hydrated and dehydrated bone beams. Difference in means significant at P<0.05 based on homoscedastic two tailed t-test. Error bars are ±1 standard deviation.

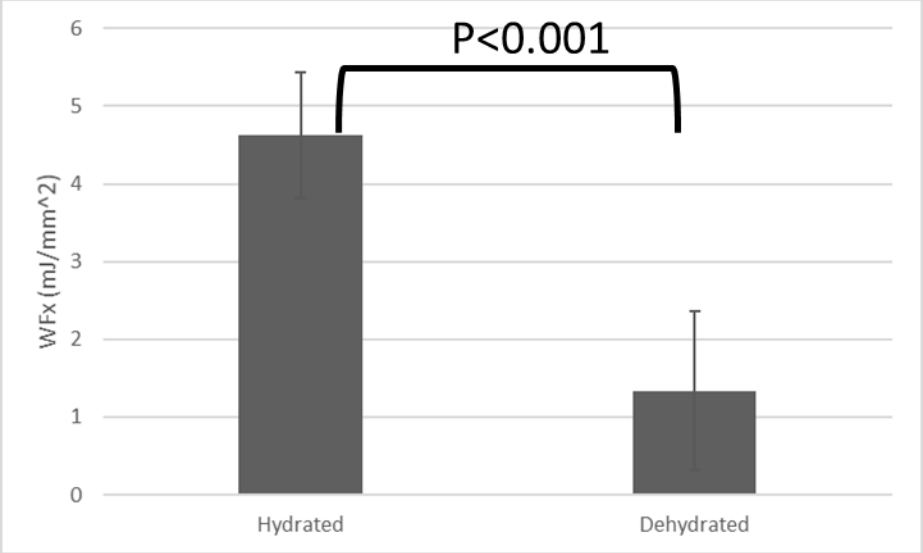

Figure 4-5: Comparison between mean WFx in hydrated and dehydrated bone beams. Difference in means significant at P<0.05 based on homoscedastic two tailed t-test. Error bars are ±1 standard deviation.

For all mechanical properties examined, the hydrated samples demonstrated significantly more overall resistance to fracture. The WFx was most affected, with the dehydrated samples dissipating 1.34±0.47 mJ/mm^2, less than a third of the mean WFx of the hydrated samples (4.63±0.81 mJ/mm^2). A drop was also seen in the comparison between peak load in both cases (96.6±40.9 N dehydrated from 159.5 ±36.8 N hydrated) and maximum deflection prior to unstable fracture (0.16±0.05 mm dehydrated from 0.28 ±0.02 mm hydrated). Additionally, the hydrated samples could undergo stable crack extension whereas none of the dehydrated samples could.

4.1.2 Comparison between notch area and mechanical behavior

To determine if the variance between notches had an impact on test behavior, the max load, max displacement, and WFx of these specimens was tested for correlation to notch area, and the significance of that correlation was recorded. The R^2 and P value for each relationship in the hydrated beams is shown in Table 1 below.

Table 1: Relationship between mechanical behavior and notch area in hydrated bone beams.

Correlated variable	R^2	P value
Max Load (N)	0.3602	0.16
Max Displacement (mm)	0.0089	0.86
WFx (mJ/mm^2)	0.1261	0.49

In the hydrated bone tests, there were no statistically significant correlations between mechanical behavior and notch area. A similar analysis for the dehydrated bone beams is shown below in Table 2.

Table 2: Relationship between mechanical behavior and notch area in dehydrated bone beams.

Correlated variable	R^2	P value
Max Load (N)	0.107361	0.106
Max Displacement (mm)	0.467	0.2
WFx (mJ/mm^2)	0.894	0.015

Interestingly, there was a statistically significant correlation between WFx and fracture surface area. The relationship observed in the dehydrated samples is negative ($R=-0.94$), suggesting that samples with a larger fracture surface area required less work per unit of fracture surface area to propagate a fracture through the beam during mechanical testing. One reason this may have happened is that WFx is normalized to surface area of the fracture surface, but within the bounds of this experiment the increase in area may not have contributed substantially to the energy needed to propagate a fracture through the dehydrated samples.

As a final comparison the mean notch area was compared between both groups.

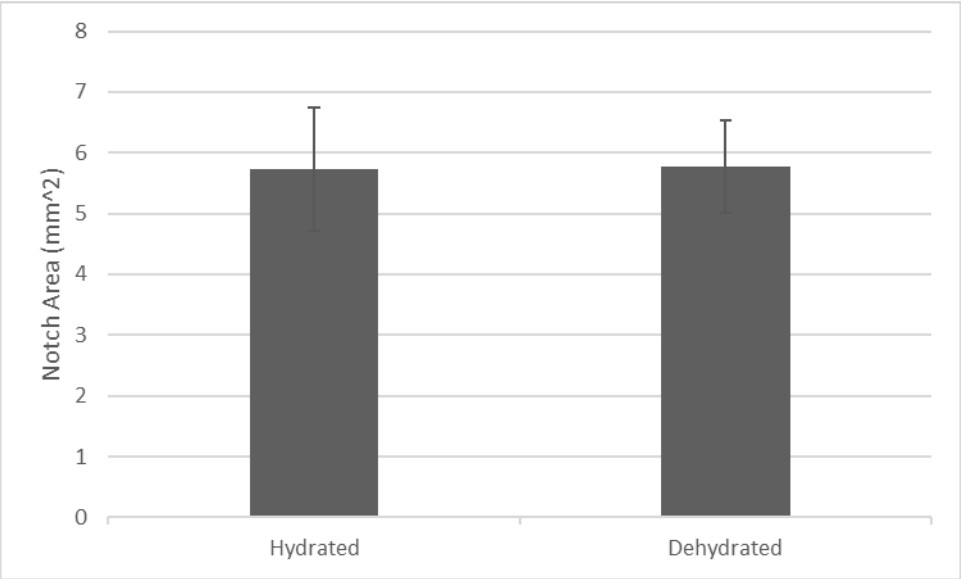

Figure 4-6: Comparison between mean notch area in hydrated and dehydrated bone beams. N = 6 for each bar. Difference in means was not significant with P>0.05 based on homoscedastic two tailed t-test. Error bars are ±1 standard deviation.

While there was some variance in notch cutting, the chevron notches were overall very consistent between the test groups. The mean fracture surface area in the hydrated group was 5.73±1.01 mm^2 and 5.78 ± 0.68 mm^2

4.2 Fluorescence analysis

4.2.1 Analysis of fluorescently stained control surfaces

As described in 3.5.1, the MPI of the control images were calculated, the figure below shows the comparison of all polished controls to all unpolished controls.

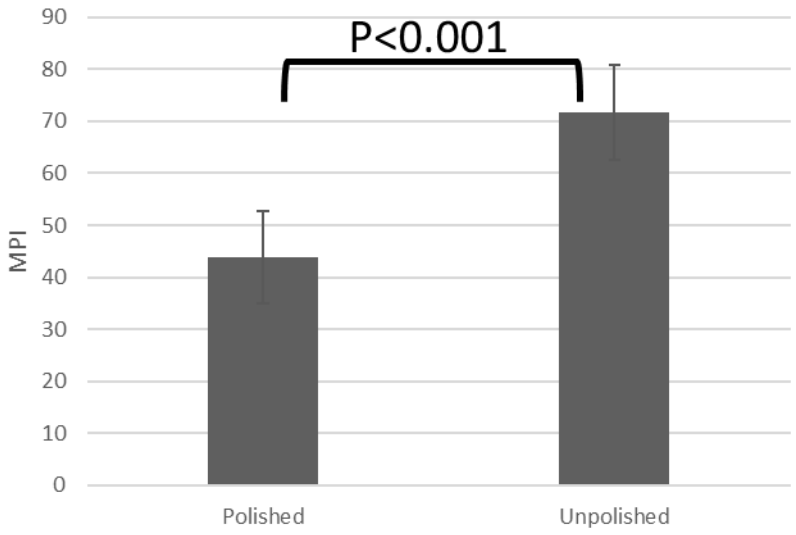

Figure 4-7: Comparison between polished and unpolished controls. P<0.05 evaluated with a paired two tailed t-test. Error bars equal to ±1 standard deviation. n =12 for each bar.

This difference is statistically significant and shows broadly that damage caused by the cutting action of the metallurgical saw is distinguishable from background levels of staining. There is a non-negligible amount of staining on the polished surface. Polishing the surface of the bone removes the damaged face produced by cutting, so the staining on that surface is not attributable to the action of the metallurgical saw. A few possible explanations for the background staining are 1) collagen that naturally exists in an unwound state within the bone matrix, 2) a result of the demineralization and staining procedure, or 3) some trace non-specific adsorption of the F-CHP. Splitting the graph to compare controls from the hydrated and dehydrated controls separately leads to very similar conclusions as shown in the figure below.

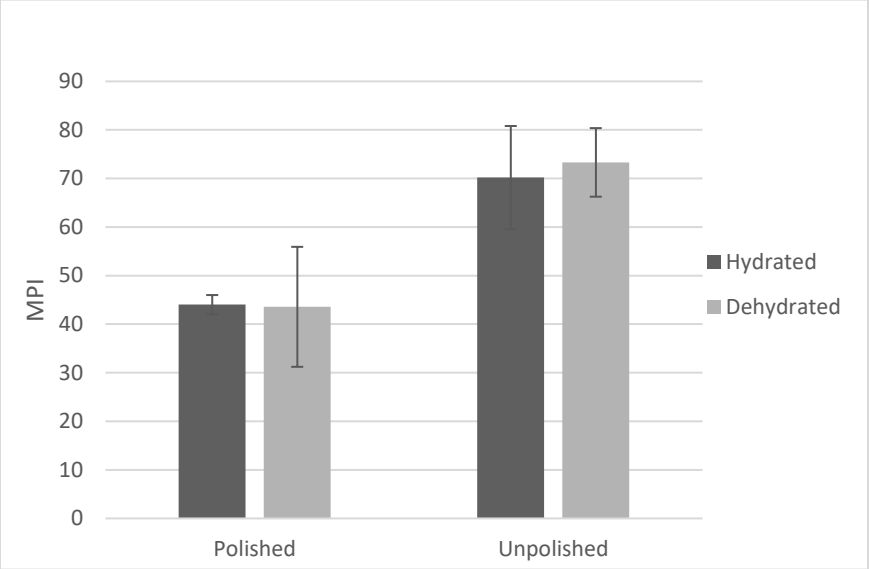

Figure 4-8: Chart comparing mean pixel intensities (MPIs) of hydrated and dehydrated controls separately. P<0.05 for both pairs. n = 6 for each bar. Error bars equal to ±1 standard deviation.

MPI effectively captures an overall increase in staining in response to damage, but more interesting is localizing the damage within the sample. As described in 3.5.1, thresholds were calculated based on the negative 'polished' controls. The hydrated sample thresholds are shown in the table below. The 99.5% threshold is provided for comparison, the median 99.95% threshold was used for additional calculations. The median was used to get a reasonable figure for aggressively removing background signal.

Table 3: Thresholds for hydrated samples.

Sample	polished 99.5% threshold	polished 99.95% threshold
1-2	61	105
1-4	68	126
1-6	65	117
2-2	83	128
2-4	67	129
2-6	64	101
median	66	121.5

Threshold values must be entered as an integer in ImageJ, so 121.5 was rounded up to 122.

Below is a table of threshold values for all dehydrated samples.

Table 4: Thresholds for dehydrated samples.

Sample	polished 99.5% threshold	polished 99.95% threshold
1-1	65	115
1-3	40	58
1-5	38	50
2-1	82	117
2-3	71	102
2-5	84	106
median	68	104

These samples overall had slightly dimmer thresholds. The 99.95% threshold was used as described previously in image analysis. The following figures show the hydrated control images from bone 1 prior to applying the 99.95% threshold.

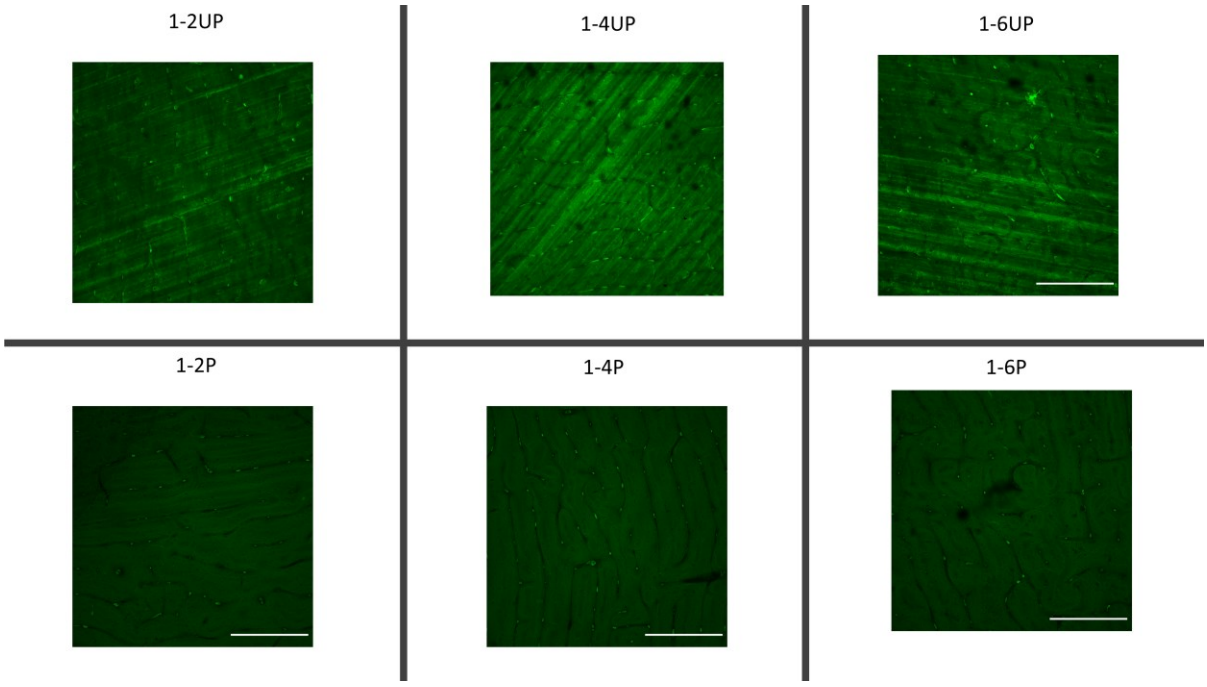

Figure 4-9: Hydrated control images from bone 1 prior to thresholding. The bottom row are polished samples (indicated as 'P)', the top row are unpolished samples (indicated as 'UP'). Scale bars are all 500 micrometers.

These bone samples all appear to be plexiform, with no well-defined osteons visible. This is expected for bovine bone [34]. The hydrated samples from bone 1 after thresholding are shown below for comparison.

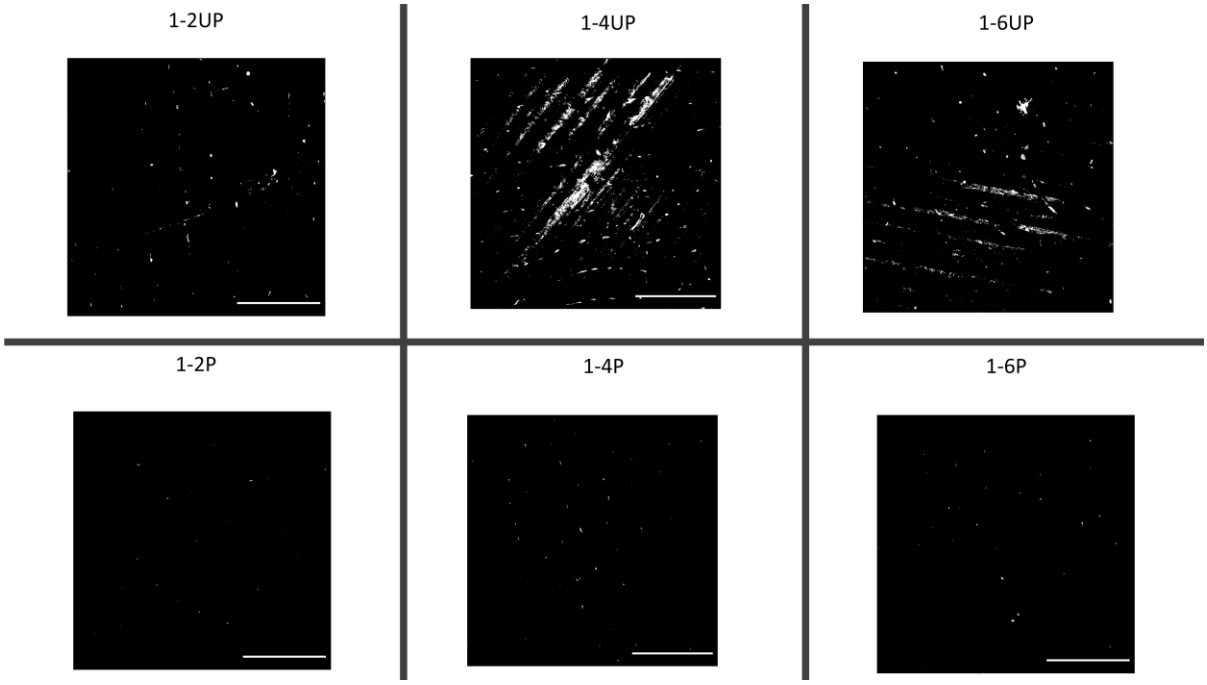

Figure 4-10: Hydrated control images from bone 1 after thresholding. The bottom row are polished samples (indicated as 'P)', the top row are unpolished samples (indicated as 'UP'). Scale bars are all 500 micrometers.

There is a clear separation between unpolished specimens and polished specimens in terms of staining above the threshold level. Distinct parallel marks from the cutting can be seen on the unpolished samples (particularly 1-4 and 1-6). This indicates that the threshold is isolating mechanical damage from background staining in the unpolished controls. The dots above threshold on the polished samples appear to be from blood vessels staining more than the surrounding bone matrix. The images from bone 2, and the dehydrated controls are presented in Appendix B as Figure A-1-to Figure B-6 These controls show the same results as above.

4.2.2 Fracture surface images

Fracture surfaces before and after thresholding are shown in the figures below, starting with hydrated samples. Image labels correspond to plot labels in Figure 4-1. All scale bars are 500 microns, fracture

surfaces are oriented with the location of tip of the fracture surface, where the fracture initiated, pointing towards the bottom of the page. Thresholded images on right, no threshold on left. Pixels that are above threshold (represented as white) are above the threshold level in the thresholded image. Red circle with arrow indicates origin of fracture and direction of propagation, red lines outline the triangular fracture surface, blue line shows the edge of the rough textured ROI used for calculating BPD. Figure 4-11-Figure 4-16 below show the hydrated fracture surfaces; threshold level was 122 based on Table 3.

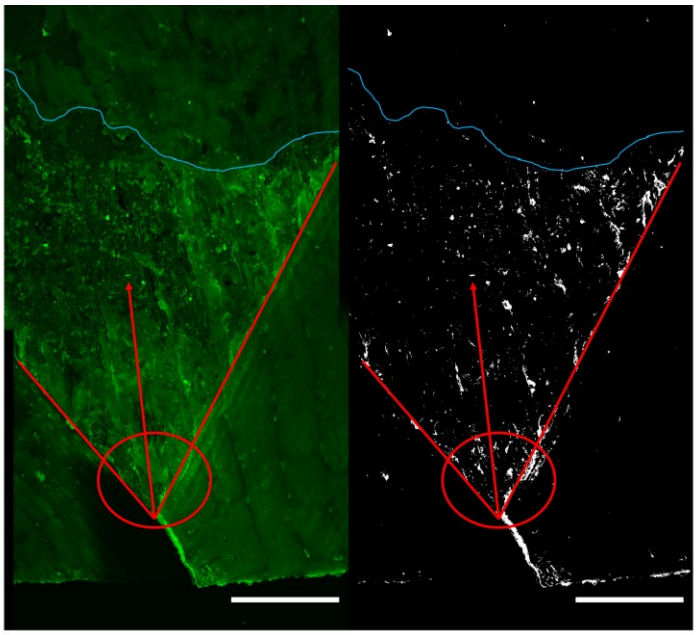

Figure 4-11: Fracture surface from 1-2. Thresholded surface on right, no threshold on left. Pixels that are above threshold (represented as white) are above the threshold level in the thresholded image. Red circle with arrow indicates origin of fracture and direction of propagation, red lines outline the triangular fracture surface, blue line shows the edge of the rough textured ROI used for calculating BPD.

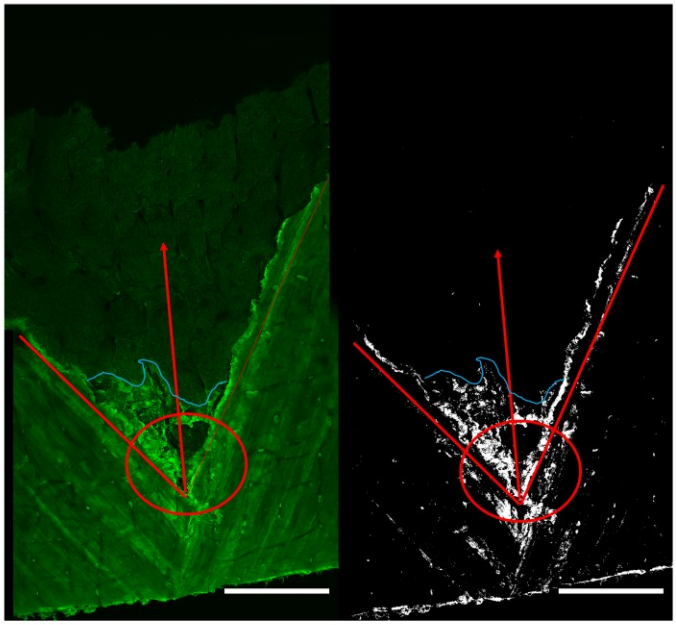

Figure 4-12: Fracture surface 1-4. Thresholded surface on right, no threshold on left. Pixels that are above threshold (represented as white) are above the threshold level in the thresholded image. Red circle with arrow indicates origin of fracture and direction of propagation, red lines outline the triangular fracture surface, blue line shows the edge of the rough textured ROI used for calculating BPD.

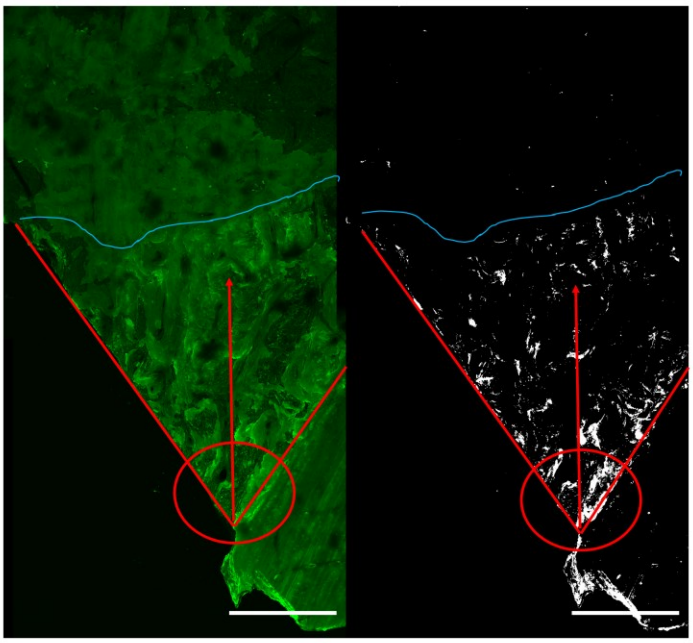

Figure 4-13: Fracture surface 1-6. Thresholded surface on right, no threshold on left. Pixels that are above threshold (represented as white) are above the threshold level in the thresholded image. Red circle with arrow indicates origin of fracture and direction of propagation, red lines outline the triangular fracture surface, blue line shows the edge of the rough textured ROI used for calculating BPD.

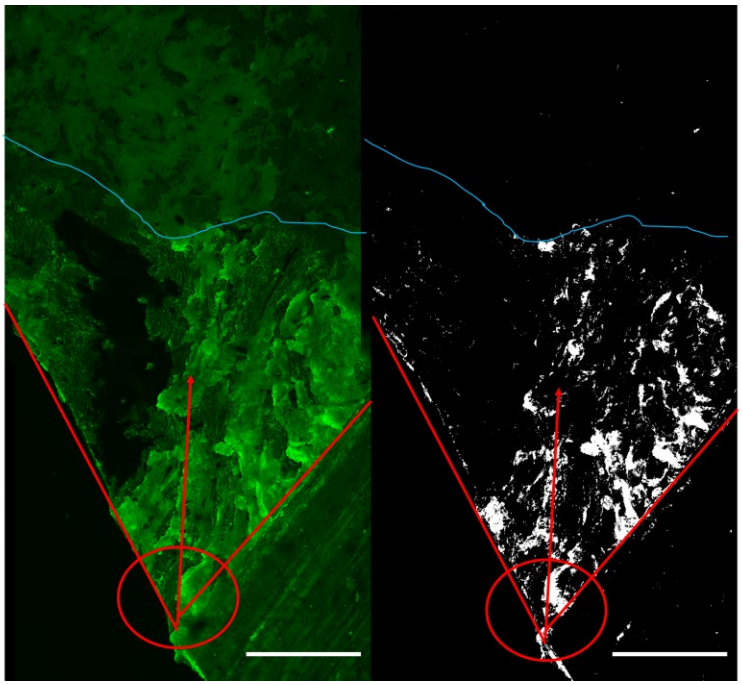

Figure 4-14: Fracture surface 2-2. Thresholded surface on right, no threshold on left. Pixels that are above threshold (represented as white) are above the threshold level in the thresholded image. Red circle with arrow indicates origin of fracture and direction of propagation, red lines outline the triangular fracture surface, blue line shows the edge of the rough textured ROI used for calculating BPD.

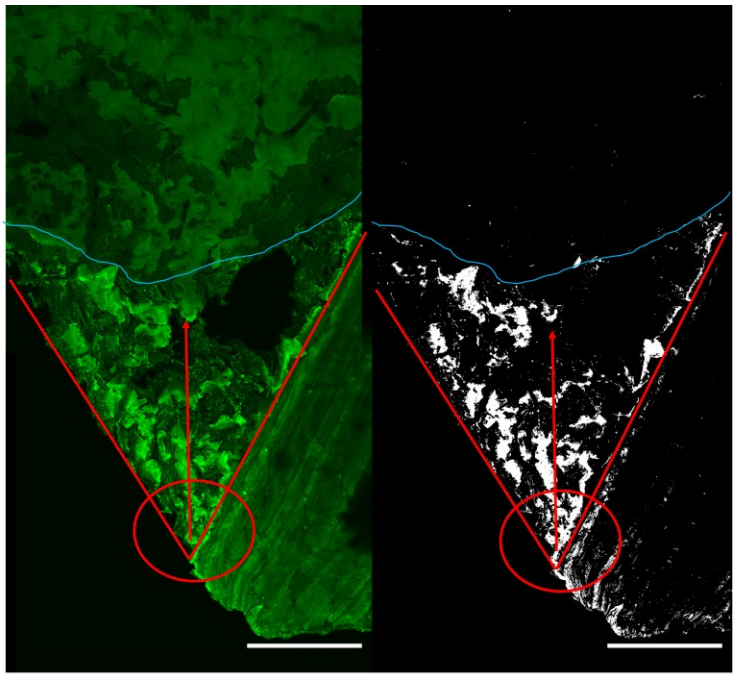

Figure 4-15: Fracture surface 2-4. Thresholded surface on right, no threshold on left. Pixels that are above threshold (represented as white) are above the threshold level in the thresholded image. Red circle with arrow indicates origin of fracture and direction of propagation, red lines outline the triangular fracture surface, blue line shows the edge of the rough textured ROI used for calculating BPD.

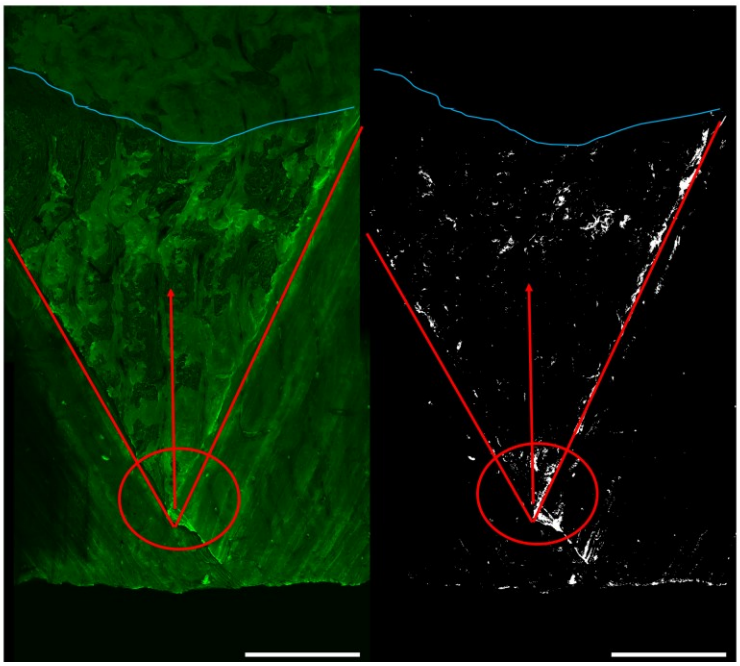

Figure 4-16: Fracture surface 2-6. Thresholded surface on right, no threshold on left. Pixels that are above threshold (represented as white) are above the threshold level in the thresholded image. Red circle with arrow indicates origin of fracture and direction of propagation, red lines outline the triangular fracture surface, blue line shows the edge of the rough textured ROI used for calculating BPD.

These fracture surfaces all showed a consistent region starting at the notch tip where staining was most prominent. Outside of this region there is substantially less staining. The following images are from the dehydrated fracture surfaces. The labels on these images correspond to the labels on the load deflection curves in Figure 4-2. Threshold value was 104 based on Table 4. As before the red circle with arrow indicates fracture origin and propagation direction. The other red lines indicate the boundaries of the triangular fracture surface.

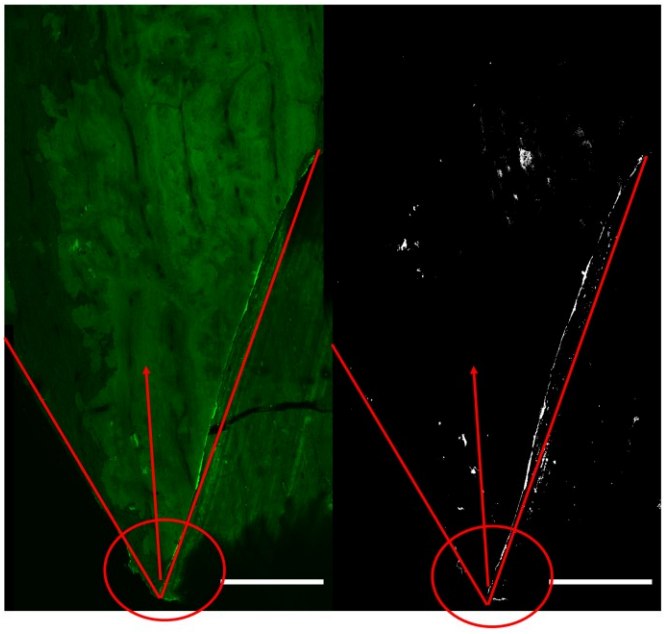

Figure 4-17: Fracture surface 1-1. Thresholded surface on right, no threshold on left. Pixels that are above threshold (represented as white) are above the threshold level in the thresholded image. Red circle with arrow indicates origin of fracture and direction of propagation, red lines outline the triangular fracture surface.

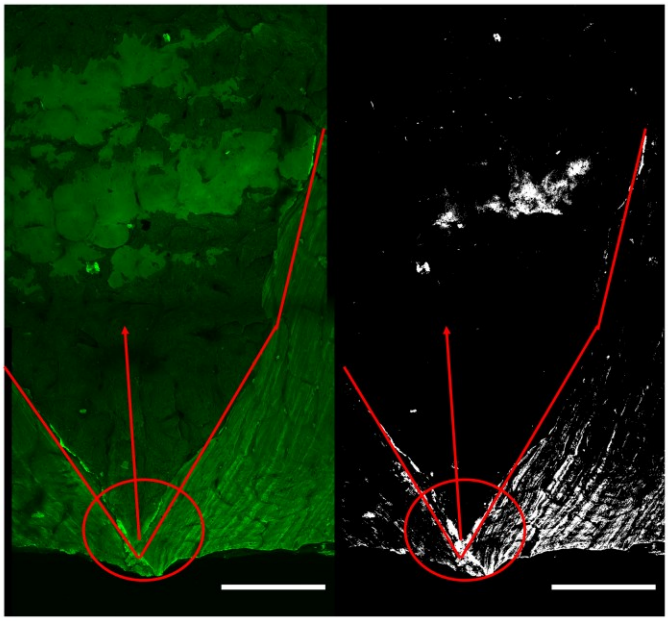

Figure 4-18: Fracture surface 1-3. Thresholded surface on right, no threshold on left. Pixels that are above threshold (represented as white) are above the threshold level in the thresholded image. Red circle with arrow indicates origin of fracture and direction of propagation, red lines outline the triangular fracture surface.

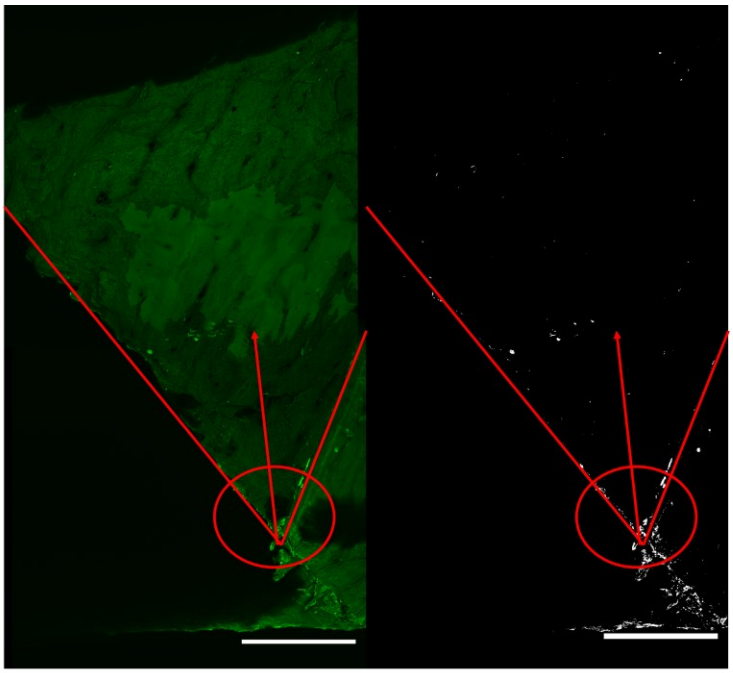

Figure 4-19: Fracture surface 1-5. Thresholded surface on right, no threshold on left. Pixels that are above threshold (represented as white) are above the threshold level in the thresholded image. Red circle with arrow indicates origin of fracture and direction of propagation, red lines outline the triangular fracture surface.

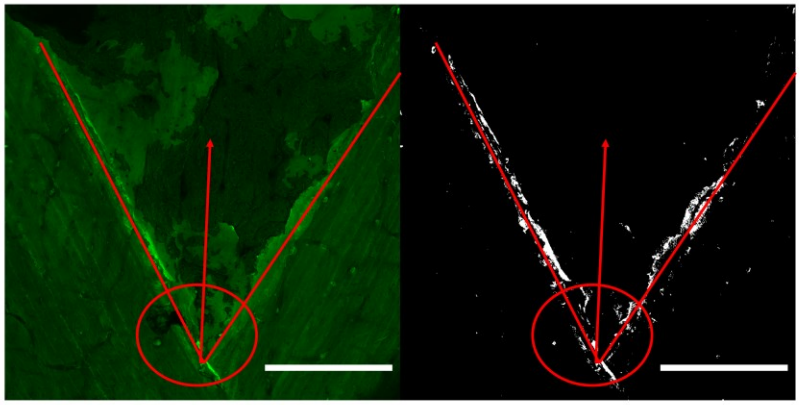

Figure 4-20: Fracture surface 2-1. Thresholded surface on right, no threshold on left. Pixels that are above threshold (represented as white) are above the threshold level in the thresholded image. Red circle with arrow indicates origin of fracture and direction of propagation, red lines outline the triangular fracture surface.

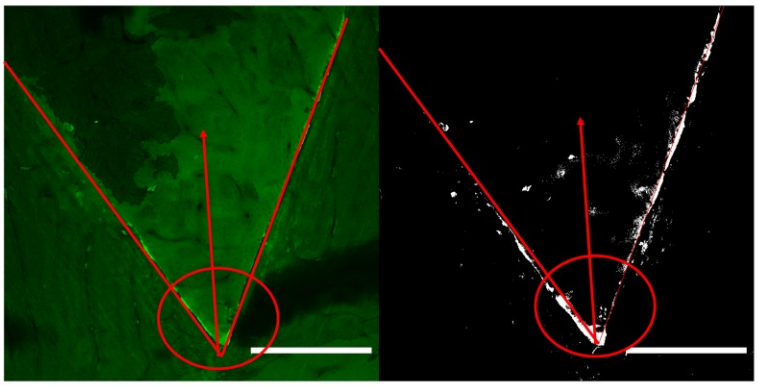

Figure 4-21: Fracture surface 2-3. Thresholded surface on right, no threshold on left. Pixels that are above threshold (represented as white) are above the threshold level in the thresholded image. Red circle with arrow indicates origin of fracture and direction of propagation, red lines outline the triangular fracture surface.

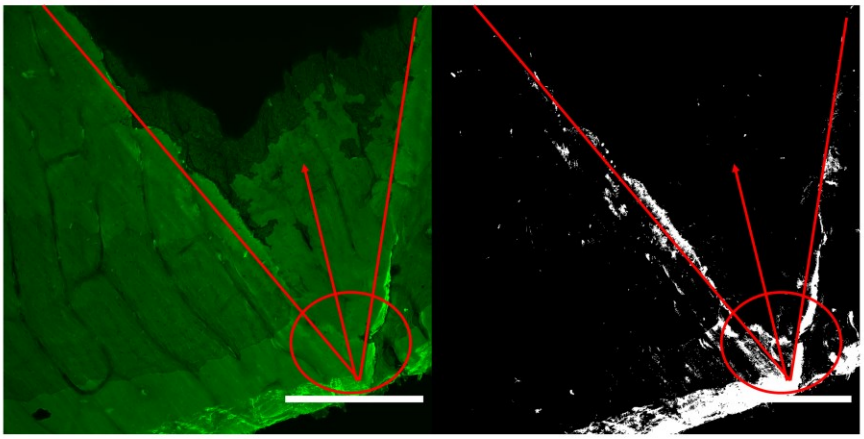

Figure 4-22: Fracture surface 2-5. Thresholded surface on right, no threshold on left. Pixels that are above threshold (represented as white) are above the threshold level in the thresholded image. Red circle with arrow indicates origin of fracture and direction of propagation, red lines outline the triangular fracture surface.

The hydrated and dehydrated fracture surfaces have notable qualitative differences in appearance. Dehydrated fracture surfaces do not have a consistent region of increased staining around the region of crack initiation and minimal staining over threshold is found within the chevron notch. The dehydrated samples had a smaller region scanned because of microscope time constraints.

Some fracture surfaces, such as 1-5, only have one side of the chevron notch visible. This is an indicator of poor alignment of the cutting plane of the chevron notch. Since the chevron notch was made with two cuts, it is possible for one cut to be slightly 'above' the other. In this case, for one side of the notch to not be visible, the misalignment between cuts would be ~100 μm. This represents a potential source of variance in mechanical behavior. Even so, hydrated samples with misaligned notches displayed stable crack extension.

4.3 Relationships between staining and fracture behavior

Qualitative analysis of the fracture surfaces shows that the hydrated samples, which had more stable behavior, stained more than the dehydrated samples with no stable behavior. It is also clear from the images that the hydrated samples did not all stain equally. The WFx was plotted against the BPC and BPD to determine if there was a relationship.

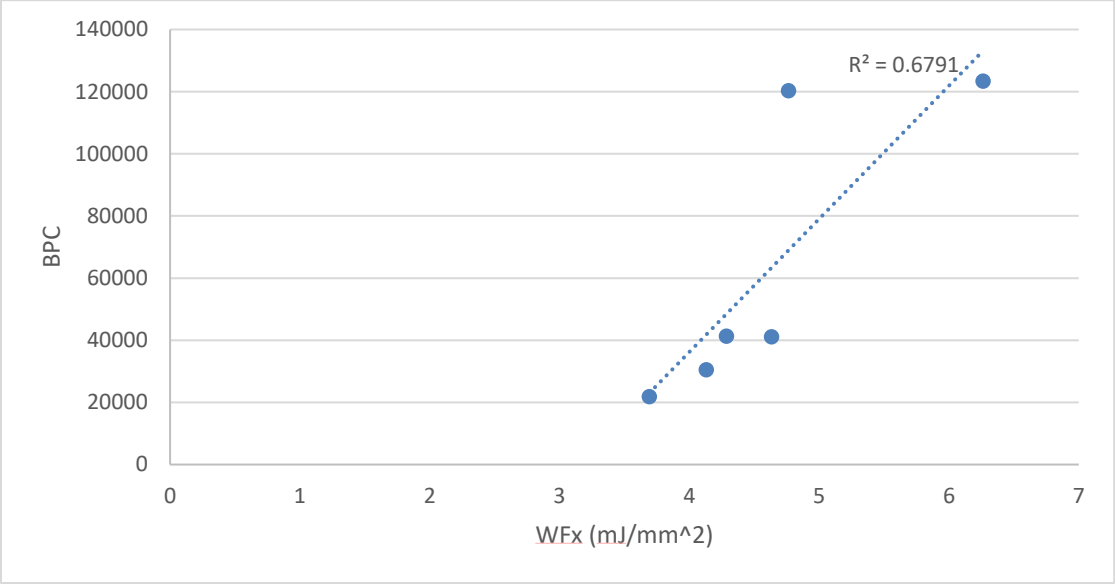

Figure 4-23: Comparison between WFx and bright pixel count (BPC) in hydrated Samples. Correlation between bright pixel count (BPC) and WFx is statistically significant with P<0.05.

Here, it is shown that there is a statistically significant correlation (R^2 =0.6791) between pixels above threshold and the work done to fracture the sample. The BPD and WFx has a stronger correlation (R^2 =0.8868) as shown in Figure 4-24 below. 1-4 was excluded from this figure and other BPD based analysis because of its outlier behavior as an unstable fracture, resulting in a small ROI, which would lead to a BPD disproportionate to the total staining.

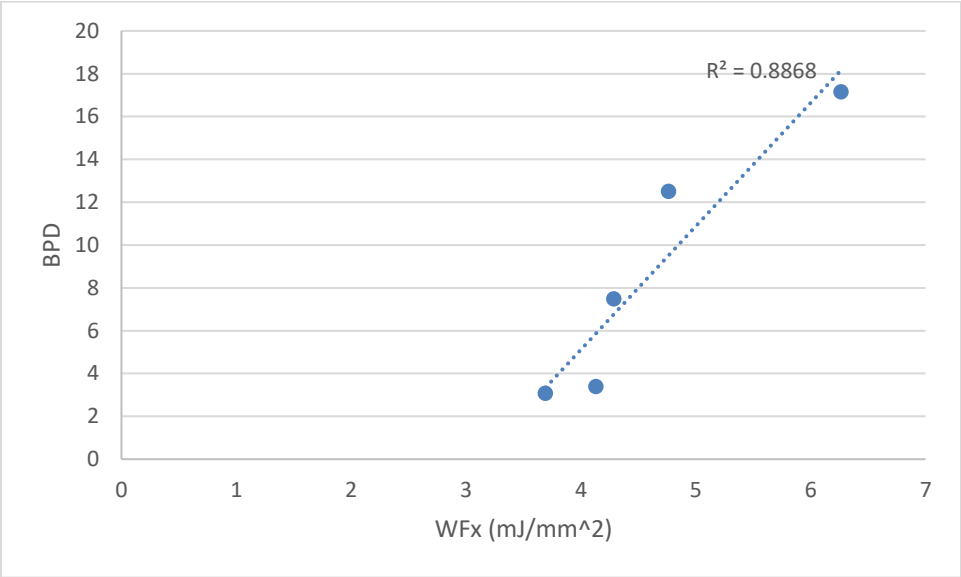

Figure 4-24: Comparison between WFx and bright pixel density (BPD) in hydrated samples. Correlation between bright pixel density (BPD) and WFx is statistically significant with P<0.05. 1-4 is excluded.

The relationship between BPD and WFx in dehydrated samples is presented below. There is no statistically significant relationship. 2-5 is excluded because of high crack deflection, which caused the fracture to travel outside of the notch.

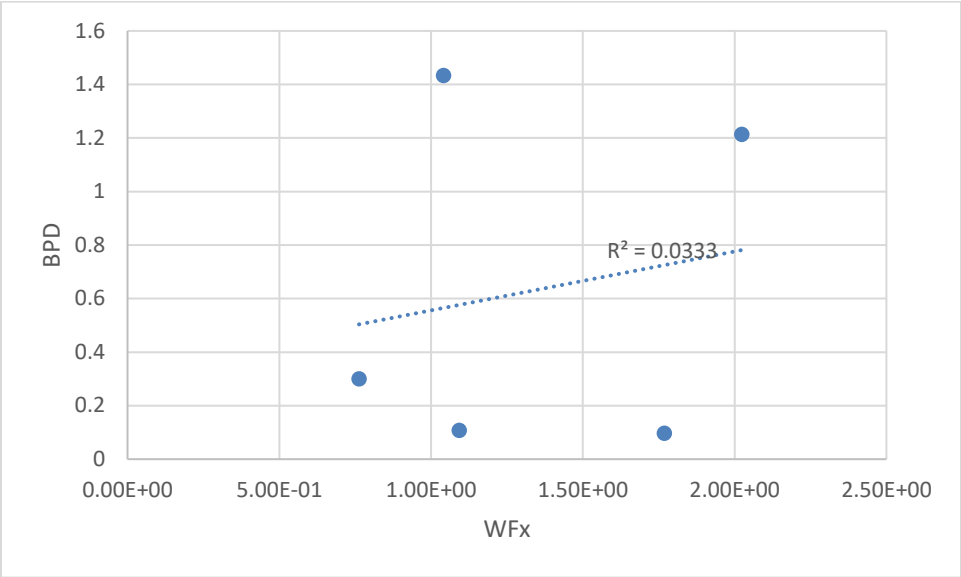

Figure 4-25: Comparison between WFx and BPD in dehydrated samples. Correlation is not significant P>0.05. 1-5 Excluded.

The figure below shows the WFx compared to BPD on a single graph for all samples.

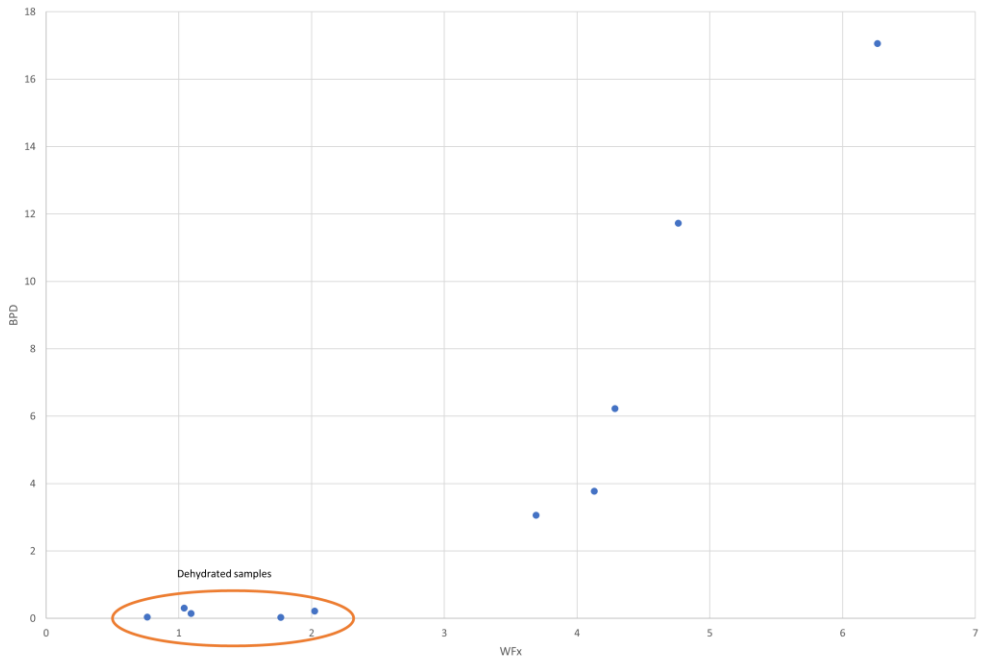

Figure 4-26: Relationship between WFx and BPD for all samples.

For this plot the threshold used for the dehydrated samples was raised from 104 to 122, based on the hydrated controls for consistent comparison. This shows that overall, not only did the dehydrated samples not have any correlation between staining and WFx but also that the staining on the fracture surface was quantitatively weaker. The mean BPD in the hydrated samples was 8.4±5.3% and 0.14±0.1%.

4.4 Comparison between F-CHP stain and SEM

Qualitative comparison between SEM images of a fracture surface and a corresponding stained surface shows a similar region of denaturation visible on both. The figure below shows this comparison. Red circle with arrow indicates origin of fracture and direction of propagation, red lines outline the triangular fracture surface, blue line shows the edge of the rough textured ROI.

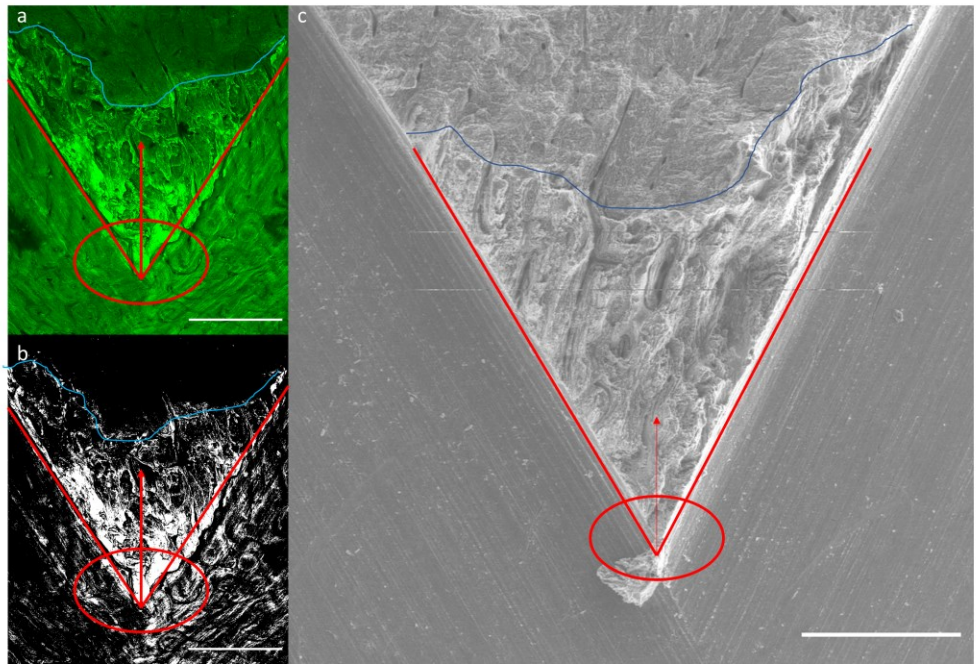

Figure 4-27: Comparison between fracture surface under SEM and F-CHP staining. Red circle with arrow indicates origin of fracture and direction of propagation, red lines indicate boundary of fracture surface, blue line indicates transition from stable to unstable crack extension in each image. Thresholding based on polished control. a) F-CHP image. b) F-CHP

image after thresholding. c) SEM image of opposite fracture surface. All scale bars 500 microns Image a is cropped and brightness has been increased for clarity. Image b is cropped for clarity.

Uncropped images without brightness adjustment are available in appendix B as Figure A-9, as well as the fluorescently stained control surfaces.

4.5 Qualitative results from human bone staining.

Two beams from a human tibia were stained as a comparison to bovine results. The figure below shows the human bone relative to its controls. First is the proximal fracture.

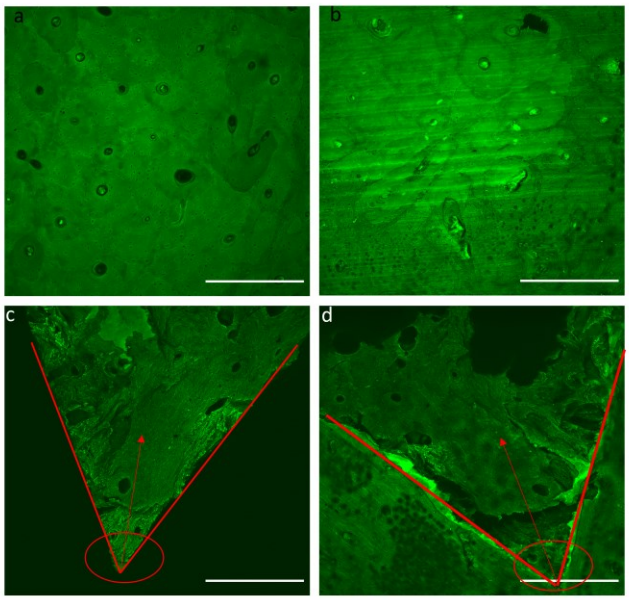

Figure 4-28: F-CHP stained human femur Bone. proximal beam. a) Polished control. b) Unpolished control. c, d) Fracture surface with red circle and arrow indicating origin of fracture and direction of propagation and the red lines indicating boundary of fracture surface. All scale bars 500 microns. Brightness adjusted for clarity in all images.

The polished and unpolished controls for this bone appear to be more Haversian than the bovine bone surfaces, as expected [34]. The same specimens after thresholding are shown below.

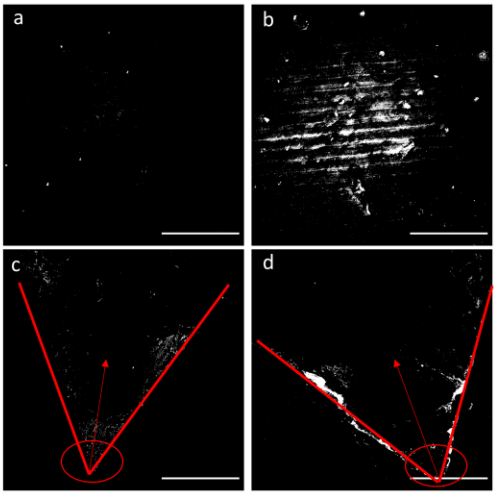

Figure 4-29: F-CHP Stained human femur Bone. Proximal beam. a) Polished control. b) Unpolished control. c, d) Fracture surface with red circle and arrow indicating origin of fracture and direction of propagation and the red lines indicating boundary of fracture surface. All scale bars 500 microns. Threshold set based on image c in Figure 4-28.

Below is the force displacement curve for this beam. Overall while there is staining above the threshold level it is relatively limited. This is a surprise given that human bone is more collagenous, and generally has a higher WFx than bovine bone [40]. The staining profile in d) is also a surprise, as it is unique in having some amount of stable tearing and staining that is almost entirely on the fringe of the fracture surface.

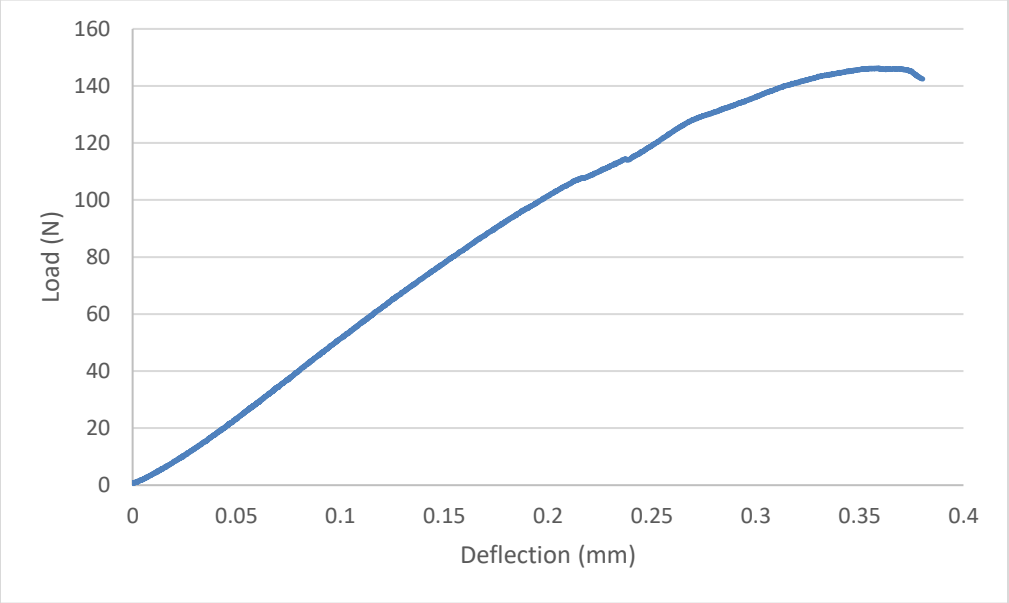

Figure 4-30: Load deflection curve for proximal human femur bone beam.

The following figure shows the distal beam from the same femur.

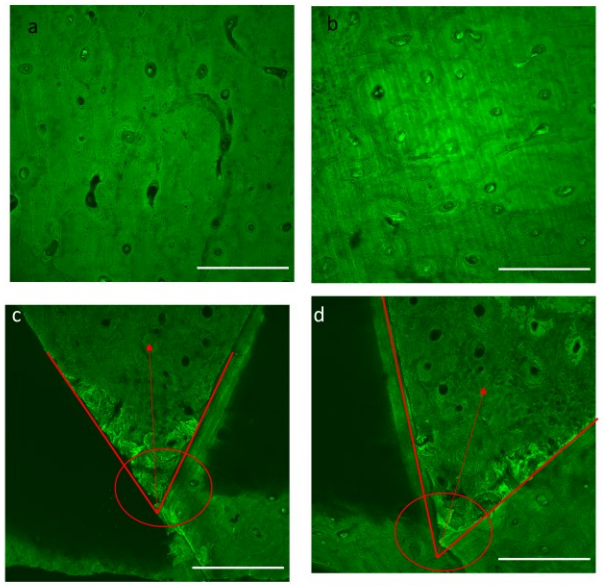

Figure 4-31: F-CHP Stained human femur bone. Distal beam. a) Polished control. b) Unpolished control. c, d) Fracture surface with red circle and arrow indicating origin of

fracture and direction of propagation and the red lines indicating boundary of fracture surface. All scale bars 500 microns. Brightness adjusted for clarity in all images.

The thresholded version of these images are shown below.

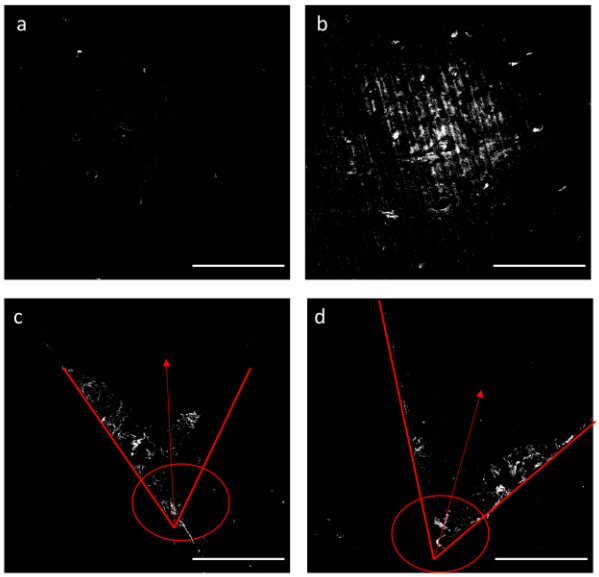

Figure 4-32: F-CHP Stained human femur Bone. Distal beam. a) Polished control. b) Unpolished control. c, d) Fracture surface with red circle and arrow indicating origin of fracture and direction of propagation and the red lines indicating boundary of fracture surface. All scale bars 500 microns. Threshold set based on image c in Figure 4-31.

These images show that the staining above background levels was primarily near the initiation site of fracture. The load deflection curve for the distal beam is shown below. This behavior is somewhat similar to sample 1-4 shown in Figure 4-12 shown previously.

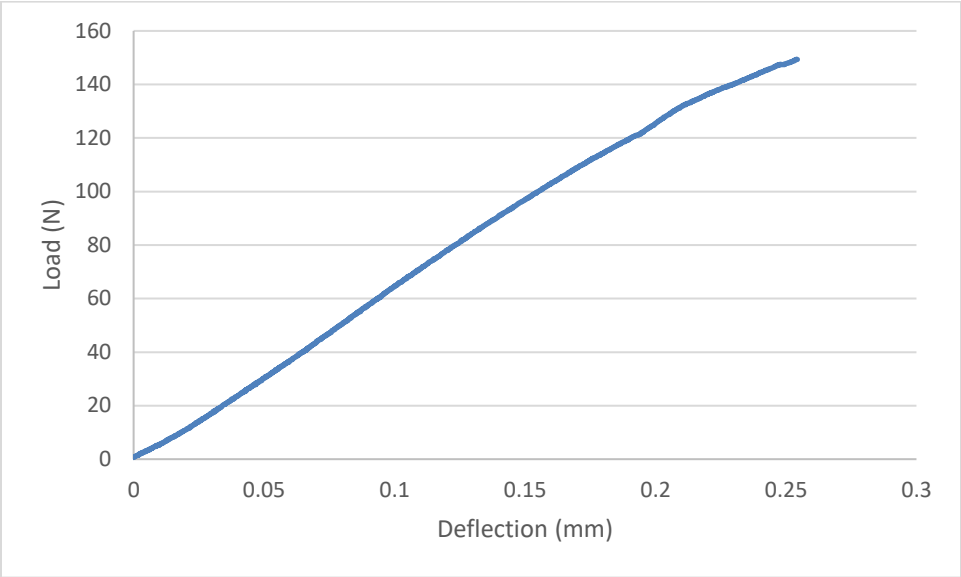

Figure 4-33: Load deflection curve for distal human femur beam.

All human bone images prior to brightness adjustment are provided in Appendix B in Figure A-7 and Figure A-8.

This behavior is somewhat similar to sample 1-4 shown in Figure 4-12 shown previously. In the sense that both samples had a relatively unstable fracture and a small region with denatured collagen visible near where the fracture initiated.

Both these human bone beams performed were less stable than expected, with either no clear stable crack extension (distal) or minimal stable extension (proximal) and while there was staining attributable to fracture on the fracture surfaces it appears more diffuse than the bovine bones.

Chapter 5
Discussion

5.1 Comparison of behavior of dehydrated and hydrated bovine bone fractured under 4-point bending

Compared to the dehydrated bone, the hydrated bone consistently performed much better in terms of WFx, maximum load and displacement to failure. Dehydrated bone samples have been very consistently observed to sustain far less deflection prior to failure when compared to hydrated bones [64], [75]. The decrease in max load before failure in the dehydrated samples is an interesting result. A decrease in max load prior to failure is consistent with other past research as dehydration been reported as decreasing max loads before failure and fracture toughness in bovine bone [56]. The mean WFx in this work was 4.63±0.81 mJ/mm^2. Notably this is within the range of reported WFx values for chevron notched bovine femur fractured at low displacement rates [40]. This shows that the behavior of the hydrated bovine bone was well within the bounds of prior research (Currey et al. 2019) [40]. The dehydrated bone had a mean WFx of 1.34 ±0.47 mJ/mm^2. This result overlaps with what WFx previously observed (Yan et al. 2008) in bovine cortical bone (femur) after drying at 60ºC in a vacuum oven for 24 hours (1.1±0.2 mJ/mm^2) [56]. In this work after dehydration the bone only has ~1/3 of the WFx as it did in the hydrated test. This is an expected result given the dehydration should negatively impact the bone's ability to dissipate energy during fracture. Molecular dynamics solutions have suggested that the collagen strands form hydrogen bonds with water, which ultimately is a lower energy and therefore an entropically favorable state [20]. When the bone is dehydrated, there is no water to solvate the collagen strands in favor of the denatured state. This would prevent collagen from dissipating energy from fracture through mechanical denaturation, leading to the experimentally observed drop in WFx.

5.2 Polished and unpolished controls

The control samples had two critical functions. First, they provided a threshold level to evaluate denaturation of collagen on the fracture surfaces, and second, they confirmed that the staining was detecting damage to the collagen molecular structure in cortical bone. Both of these functions were essential to generating meaningful data from fracture surfaces. Without a metric for damaged vs. undamaged collagen, it would be difficult to provide any salient quantitative analysis.

There is some amount of signal visible in the polished specimens. This was consistently observed, in both human and bovine controls. A few possible explanations were briefly discussed in 3.5.1. One potential explanation might be tissue autofluorescence. Whole bone can fluoresce in the range around 512 nm where F-CHP has its emission peak [76], [77]. This is unlikely to explain the signal observed in this experiment because it requires UV excitation, which would not be provided by a 488 nm argon laser [76], [77]. This could also be a byproduct of adsorption, as collagen naturally adsorbs onto hydroxyapatite and F-CHP deliberately mimics this structure [78]. That said the total amount of adsorption should be somewhat constrained by the 5 washes performed before imaging, which should limit the amount of loosely adsorbed material remaining. Additionally, the samples were all partially demineralized, which should have removed any hydroxyapatite from the surface being imaged. One other possibility is the presence of denatured bone naturally within the bone matrix. Raman microscopy studies have seen biomarkers associated with collagen denaturation, namely the ratio between 1640 cm^{-1} and 1670 cm^{-1} Raman shift peaks, present in undamaged bovine bone [79]. This might suggest that naturally in bovine bone some F-CHP staining should be expected from some baseline quantity of denatured collagen.

The significant increase in signal observed due to the cutting compared to the natural structure shows that mechanical damage can be detected above this background level. As a result, a threshold level that distinguished excess collagen denaturation as a byproduct of fracture could be identified. On the fracture surface, the signal above the threshold cannot be attributed to baseline levels of denatured collagen in bone, because if it was, it would be below the threshold level. Furthermore, the staining cannot be attributed to the cutting action of the metallurgical saw creating the notch, because the fracture surface is not produced by the metallurgical saw. An increase in signal observed on the bone fracture surfaces, above the threshold level, must therefore be a product of the fracture process.

5.2.1 Fluorescent microscopy comparison of hydrated and dehydrated fracture surfaces

Aside from dissipating more energy prior to fracture, the hydrated bovine bone also showed more damage to collagen had occurred based on F-CHP staining. Prior research (Gautieri et al. 2009) has suggested in simulations that collagen forms more hydrogen bonds with free water when it is denatured [20]. Additionally, studies using Raman spectral analysis have reported positive correlations between markers of disorder in collagen and markers of matrix bound water and markers

of collagen disorder [79]. The highly brittle fracture of dehydrated bovine bone may be a result of the collagen being unable to effectively denature to dissipate energy without water present to solvate the denatured strands. This would explain why dehydrated samples had minimal signal above the threshold level. Conversely, the hydrated surfaces showed substantial staining throughout a stable crack extension ROI and little elsewhere. This indicates that during the fracture of bovine bone, the main contribution of collagen denaturation as a toughening mechanism occurred within a bounded region, and that outside of that collagen outside of that region did not contribute through denaturation to the WFx of the bone.

Within the hydrated samples, the quantity of highly and density of stained pixels, indicative of denatured collagen, correlated to the total WFx, this strongly suggests that collagen denaturation occurs as a toughening mechanism. Bone has been noted as having a microdamage process zone form (MDPZ) as it is deformed under load [11], [80]. This microdamage begins to form during bending as the tissue loses stiffness (noted by a reduction in the slope of the load displacement curve) [11]. One possibility is that the denaturation of collagen as a toughening mechanism begins with the onset of the MDPZ formation.

Fundamentally, the analysis of the fracture surfaces shows that not only collagen molecules denature during the fracture of bovine bone as a toughening mechanism, but that this toughening mechanism is strongly associated with stable crack extension and the nonlinear behavior prior to complete fracture. When the collagen is prevented from effectively denaturing, due to lack of water, the bone beams become very brittle and display no nonlinear behavior prior to fracture. The inability of collagen to contribute to fracture resistance in dehydrated bones is observed through the minimal amount of collagen staining above baseline staining levels. In Figure 4-11 to Figure 4-16, denatured collagen appears in hydrated bovine tibia beams, confirming the denaturation of collagen as a toughening mechanism. In the dehydrated fractures in Figure 4-17 to Figure 4-22 show that when no stable crack extension occurs, minimal damaged collagen appears. This implies that stable crack extension is strongly related to toughening through collagen denaturation. Interestingly fracture surface 1-4 shows staining but did not have a well-defined period of stable tearing visible from the load deflection curve but did still stain. Bone has been noted as having a microdamage process zone form (MDPZ) as it is deformed under load [11], [80]. This microdamage begins to form during bending as the tissue loses stiffness (noted by a reduction in the slope of the load displacement curve) [11]. One possibility is that the denaturation of collagen as a toughening mechanism begins with the

onset of the MDPZ formation, prior to fracture. Another possible explanation is the observed ROI on fracture surface 1-4 is the result of a shark precrack forming during loading, as is common for chevron notches [52]. This sharp precrack may have created a very small region of stability that in this particular case did not support any further crack extension, hence the failure of beam 1-4 once max load was reached.

5.3 Comparison of F-CHP staining to SEM image

SEM imagining allowed qualitative analysis of the morphology of the fracture surfaces. Past research on bovine bone has shown that samples that undergo some stable crack extension have an associated region of rough bone [52], [81]. The most useful aspect of this analysis towards this research is that Figure 4-27 shows very similar looking regions of stable crack extension. This is valuable for showing that the ROI observed on confocal microscopy is not a byproduct of the sample demineralization or staining, and that the ROI corresponds to the region of stable crack extension.

5.4 Human bone behavior compared to bovine bone behavior

Human bone was stained as a comparison to bovine bone. The objective of this test was to observe if similar behavior regarding fracture and denaturation of collagen could be observed in both human and bovine bone. The human bone in this experiment was less stable than expected. With the distal beam having no defined period of stable crack extension and the proximal beam failing very quickly after reaching peak load. Despite this, there are some very interesting similarities between these samples and the bovine experiments. First, the distal beam (Figure 4-31) appears very similar on both sides to bovine beam 1-4 (Figure 4-12) showing a small but distinct region of stable crack extension after a brittle fracture. The proximal beam behaved in a way that was fairly distinct from the bovine samples. Figure 4-28 c) has a distinct but small and diffuse region of stable crack extension both near to where fracture initiated and Figure 4-28 d) has denatured collagen primarily around the edges of the sample. The key result here is that human bone beams show corroboration of the observation of denatured collagen attributable to fracture.

There is no obvious explanation for the unstable behavior of the human bone beams tested. One possibility is that since the human bone was kept at -80ºC rather than -20ºC like the bovine bone, but still rehydrated for the same amount of time at room temperature that this may have impeded full thawing and rehydration. Potentially replicating the experiment with human bone being stored at -

20ºC prior to notching and testing or given a longer rehydration period prior to testing would result in more consistently stable behavior. Even so these samples had a rehydration time greater than 12 hours at ambient temperatures which should have been adequate for fully hydrating the bone. Future work is needed to fully understand the relationship between stable crack extension, and the mechanical denaturation of collagen as a toughening mechanism in human cortical bone.

Even with this unexpected unstable behavior, the observation of similar staining patterns on unstable human and bovine bone suggests a consistent role for collagen denaturation in the absence of stable fracture. It also demonstrates that collagen denaturation as a toughening mechanism is not restricted to bovine bone. This cross-species similarity is expected given the consistent nano-scale mineralized fiber structure of cortical bone between species [1]–[3].

5.5 Limitations

5.5.1 Fracture mechanics

All mechanical testing was done at room temperature rather than physiological temperatures. This may have impaired the ability of the mechanical testing specimens to behave in a physiological manner. A testing system that maintains the mechanical test specimens at physiological temperatures during loading could improve on the work presented here, as it would allow testing closer to the natural conditions bone operates under as a tissue.

Whether the bone beams had been fully hydrated or dehydrated was not determined in this work. It was assumed that after the drying or hydration time that the samples would have reached relatively complete drying or hydration. It is possible for example, that a longer period of dehydration, might have resulted in even more changes to the material behavior of bone than was observed.

A relatively simple fracture mechanics approach was applied in this thesis research. The most important mechanical characteristic analyzed from the bone fracture is WFx. This metric does not make adjustment for the specific notch geometry of each sample. Functionally, this assumes that the differences between samples are not causative factors in the differences between samples in this experiment. Fracture toughness (Kvb or Kc) is a commonly-used metric for fracture toughness that has been used in prior research (Yan et al. 2006) and takes into account specimen geometry [52]. This metric is not very practical for this work. Calculating Kvb for a chevron notched test requires a well-defined period of stable fracture extension [51]. In this work none of the dehydrated samples

underwent any stable crack extension. Furthermore, the notches were modified for ease of use, making them non-compliant with ASTM C1421-18. Prior research (Zioupos et al. 2020) with chevron notched bone beams has used notch geometries outside of ASTMC1421-18 [16]. In research focusing on comparisons between ductile and brittle transitions, the fracture toughness is often omitted [13], [16], [40]. A notable defect, that could have impacted fracture behavior was misalignment of the two cuts used to form the notch. Not having the notch well aligned will impact how stresses are distributed within in the samples, and consequently could have impacted how they fractured. While this is a limit to the analysis of fracture behavior it does not impede the overall comparison of energy dissipation to F-CHP staining. Additionally, since stable and unstable behavior can be easily distinguished directly from a load-displacement curve it remains possible to make analysis based on that behavior. Furthermore, even if there was an undetected relationship between notch inconsistencies and stable crack extension, it still would have still allowed observation of the relationship between the fracture behavior and the resultant F-CHP staining.

5.5.2 Optical instrumentation

Laser scanning confocal microscopy is a powerful tool for analyzing fracture surfaces but does have its limitations. In Figure 4-15, for example, there is a 'gap' present in the region of interest with no signal. It is possible that there is F-CHP staining in this region that was not captured by this imaging. This is because the microscope attenuates all signal outside of the depth of field [82]. A larger pinhole can mitigate this but may have the side effect of having unfocused signal leading to a more blurry image [82]. The airy 1 pinhole setting used here is a common compromise that allows for an optical slice thick enough for most work, while also maintaining a sharp image [82]. As is visible from the images in this report, the pinhole settings were adequate for creating well-resolved images. Since the hydrated surfaces with the most rough ROIs were the most highly stained (Figure 4-14, Figure 4-15), this would have biased the experiment to underestimate the staining and thus towards failing to detect a relationship between fracture behavior and staining. It is possible that the true relationship between denatured collagen and WFx is stronger than the statistically significant correlation shown in Figure 4-23

Another limitation of confocal based analysis is that while the quantity of denatured collagen present is proportional to the F-CHP staining the exact correlation is unknown. The molecular weight of a single collagen strand, in triple helical collagen, is ~100kDa [83]. A single strand of F-CHP has a

weight of ~2.9kDa [72]. Normally, F-CHP is blocked from binding to collagen in its native state by the tight hydrogen bonding holding the triple helix together [57]. Given the large difference in size, it is possible that multiple F-CHP probes may bind to a single denatured collagen strand without obstructing each other; Figure 2-4 shows a schematic of this happening in rat tail tendon [57]. Researchers using F-CHP have correlated the total staining to lysed collagen via hydroxyproline, an amino acid used as a proxy for collagen, to estimate the quantity of denatured collagen [84]. While this is an interesting prospect, the necessity of combining multiple fluorometric readings to calibrate this measurement increases the noise levels of the experiment [84]. What is notable is the general agreement between the two methods of assessing collagen denaturation [84]. The lack of an absolute quantity of denatured in this work prevents making claims such as "30% of the collagen molecules were in a denatured state after fracture" but it still allows relative analysis as was done with thresholding. This allows for claims such as "The rough textured ROI had an increase in denatured collagen relative to a polished control over 10% of its surface area" which is captured by BPD, or "there was an increase in the total amount of denatured collagen", which is related to BPC.

One concern regarding fluorophore use is the potential for photobleaching, where fluorescent molecules can lose their fluorescence after being excited by light [85]. Photobleaching is unlikely to have had a major impact on this study as the samples were stained in a refrigerator with no light, and neither the F-CHP stock solution, nor the stained samples were left sitting in ambient light. Samples were only scanned once with the confocal microscope. If photobleaching were a significant concern, we would expect the polished and unpolished controls to be indistinguishable, as the fluorescence would be extinguished. This was not observed.

5.5.3 Staining and sample preparation

In the methods (section 3.3), several steps were said to be done 'overnight' such as staining which was done for 25 hours for the dehydrated samples, and 18 hours for the hydrated samples. The overall agreement between the means of both polished and unpolished controls suggests that this did not introduce bias into the experiment. Bias could have been detected via a difference in the mean pixel intensity of the controls. Figure 4-8 shows that the mean pixel intensities agree very strongly between the hydrated and dehydrated experiments. This implies that the differences between these overnight steps did not impact the observed staining.

Chapter 6
Conclusions

The primary objective of this thesis project was to test the hypothesis: "**Bone collagen denatures as a toughening mechanism during the stable fracture of cortical bone**". To test this hypothesis an experiment was devised using F-CHP to stain denatured collagen so that the denaturation resulting from fracture could be detected via confocal microscopy. Based off the analysis of controls, mechanical damage from cutting showed a clear signal discernable from the natural microstructure of bone. The denatured collagen observed correlated significantly with work done on the sample. These results support the hypothesis of this work; during stable fracture of cortical bone collagen molecules denature as a toughening mechanism.

The first question presented in the motivation section was: Does the denaturation of collagen occur exclusively during stable crack extension? SEM imaging of a fracture surface showed the existence of a rough textured region consistent with prior (Yan et al. 2006) observations of stable tearing on a chevron notch [52]. The confocal image of the opposite fracture surface showed a very similar region, and that this region corresponds to the location of denatured collagen following fracture. In the hydrated fracture surfaces presented in Figure 4-11 to Figure 4-16 this stable crack extension region corresponding to the location of denatured collagen is present. This suggests that the denaturation of collagen as a toughening mechanism occurs exclusively during stable tearing.

The dehydrated bovine bone samples also answer question 2 from the motivation: Can mechanical denaturation of collagen as a toughening mechanism occur in dehydrated bone? No, collagen does not denature as a toughening mechanism in dehydrated bone. These samples have minimal staining on the fracture surface that cannot be attributed to background and this signal does not correlate to the energy dissipated by the bone.

Question 3 was, How does the quantity of denatured collagen relate to the amount of stable crack extension? The data from the hydrated bone beams suggests that there is a positive linear correlation between the quantity of denatured collagen and the amount of energy dissipated during fracture.

6.1 Future Work

6.1.1 Further exploration of the role of collagen denaturation-based toughening in cases of aging and disease

Predicting the fragility of bone in medical contexts is a consistent research challenge. Bone mineral density is one criterion used to predict the fragility in bone, and can be measured via x-ray imaging [86]. However, it is not fully predictive of bone fracture behavior [87]. Beyond mineral properties, the oxidation of collagen and non-collagenous proteins in diabetes patients has been suggested as a source of bone fragility [88]. One research question could be: "Does oxidative damage, caused in aging or disease cause bone fragility by damaging the triple helical structure of collagen?" Raman microscopy results discussed earlier have observed a correlation between markers of collagen quality and bone toughness [21]. A prediction based on this would be that if the experiment detailed in sections 3.1-3.5.2 was repeated on bone that had suffered oxidative damage that there would be no increase in staining on a fracture surface relative to a polished control from the same bone. This would show that the collagen was damaged prior to fracture, limiting its ability to engage to resist fracture.

6.1.2 Cross species comparisons

Bovine cortical bone used in this study is a fairly stiff material, highly mineralized bone [3]. Existing in sharp contrast to this is antler, a relatively poorly mineralized, but very tough bone [40], [55]. It also dissipates energy very effectively under impact loading [40]. This leads to the question: "how does the denaturation of collagen impact toughness in different species and bone types?" Bovine cortical bone as a highly mineralized bone may represent a case of relatively less overall collagen denaturation.

6.2 Contributions

This work represents the first ever direct observation of collagen denaturation as a toughening mechanism during bone fracture. This represents a concrete step forward in understanding how bone resists fracture. The F-CHP staining and imaging method represents a novel way to gain information pertaining to the molecular-level behavior of collagen during fracture. Previous researchers have observed transitions between rough and smooth areas on fracture surfaces that have been associated with stability and instability. These methods were limited by lacking the ability to determine the state

of the collagen on a molecular level. Here, these regions and transitions can be observed, and the behavior of collagen within these regions and outside of them can be assessed. Comparing the SEM and confocal results together shows that these morphological features were conserved between imaging techniques. The test with human bone expands the scope of this work beyond only using animal models. This reveals that not only is collagen denaturation a toughening mechanism in bovine bone, but that it is conserved across species, including to humans.

Prior to this work, it was known that the quality of collagen within bone matrix was a predictor of the bone's ability to resist fracture. Now, it has been conclusively demonstrated that the collagen molecules mechanically denature, absorbing energy during fracture.

Letters of Copyright Permission

Figure 2-1:

Order Date

13-Nov-2021

Order License ID

1161494-1

ISSN

1545-4118

Type of Use

Republish in a thesis/dissertation

Publisher

ANNUAL REVIEWS

Portion

Image/photo/illustration

Licensed Content

Publication Title

Annual review of materials research

Date

01/01/2001

Language

English

Country

United States of America

Rightsholder

Annual Reviews, Inc.

Publication Type

e-Journal

URL

http://arjournals.annualreviews.org/loi/matsci

Request Details

Portion Type

Image/photo/illustration

Number of images / photos / illustrations

1

Format (select all that apply)

Print, Electronic

Who will republish the content?

Academic institution

Duration of Use

Life of current and all future editions

Lifetime Unit Quantity

Up to 999

Rights Requested

Main product

Distribution

Canada

Translation

Original language of publication

Copies for the disabled?

No

Minor editing privileges?

No

Incidental promotional use?

No

Currency

USD

New Work Details

Title

Collagen Denaturation as a Toughening Mechanism in Cortical Bone

Instructor name

Thomas Willett

Institution name

University of Waterloo

Expected presentation date

2021-12-16

Additional Details

Order reference number

N/A

The requesting person / organization to appear on the license

Corin Seelemann

Figure 2-2

License Number	5180470727375
License date	Nov 01, 2021
Licensed Content Publisher	Elsevier
Licensed Content Publication	Engineering Fracture Mechanics
Licensed Content Title	Analysis of fracture processes in cortical bone tissue
Licensed Content Author	Simin Li,Adel Abdel-Wahab,Vadim V. Silberschmidt
Licensed Content Date	Sep 1, 2013
Licensed Content Volume	110
Licensed Content Issue	n/a
Licensed Content Pages	11
Start Page	448
End Page	458
Type of Use	reuse in a thesis/dissertation
Portion	figures/tables/illustrations
Number of figures/tables/illustrations	1
Format	both print and electronic
Are you the author of this Elsevier article?	No
Will you be translating?	No
Title	Collagen Denaturation as a toughening mechanism in cortical bone
Institution name	University of Waterloo
Expected presentation date	Nov 2021
Portions	Figure 1
Requestor Location	University of Waterloo 20 Abraham Ave Markham, ON L3T 5L8 Canada Attn: University of Waterloo

Publisher Tax ID	GB 494 6272 12
Total	0.00 USD

References

[1] N. Reznikov, R. Shahar, and S. Weiner, "Bone hierarchical structure in three dimensions," *Acta Biomater.*, vol. 10, no. 9, pp. 3815–3826, 2014.

[2] S. Weiner and H. D. Wagner, "The material bone: Structure-mechanical function relations," *Annu. Rev. Mater. Sci.*, vol. 28, no. 1, pp. 271–298, 1998.

[3] J. Aerssens, S. Boonen, G. Lowet, and J. Dequeker, "Interspecies differences in bone composition, density, and quality: Potential implications for in vivo bone research," *Endocrinology*, vol. 139, no. 2, pp. 663–670, 1998.

[4] M. E. Launey, M. J. Buehler, and R. O. Ritchie, *On the mechanistic origins of toughness in bone*, vol. 40. 2010.

[5] R. K. Nalla, J. S. Stölken, J. H. Kinney, and R. O. Ritchie, "Fracture in human cortical bone: Local fracture criteria and toughening mechanisms," *J. Biomech.*, vol. 38, no. 7, pp. 1517–1525, 2005.

[6] O. A. Tertuliano, B. W. Edwards, L. R. Meza, V. S. Deshpande, and J. R. Greer, "Nanofibril-mediated fracture resistance of bone," *Bioinspiration and Biomimetics*, vol. 16, no. 3, p. 35001, 2021.

[7] K. J. Koester, J. W. Ager, and R. O. Ritchie, "The true toughness of human cortical bone measured with realistically short cracks," *Nat. Mater.*, vol. 7, no. 8, pp. 672–677, 2008.

[8] K. Ioku, M. Yoshimura, and S. Somiya, "Microstructure and mechanical properties of hydroxyapatite ceramics with zirconia dispersion prepared by post-sintering," *Biomaterials*, vol. 11, no. 1, pp. 57–61, 1990.

[9] H. S. Gupta, J. Seto, W. Wagermaier, P. Zaslansky, P. Boesecke, and P. Fratzl, "Cooperative deformation of mineral and collagen in bone at the nanoscale," *Proc. Natl. Acad. Sci. U. S. A.*, vol. 103, no. 47, pp. 17741–17746, 2006.

[10] C. L. Malik, S. M. Stover, R. B. Martin, and J. C. Gibeling, "Equine cortical bone exhibits rising R-curve fracture mechanics," *J. Biomech.*, vol. 36, no. 2, pp. 191–198, 2003.

[11] T. Willett, D. Josey, R. X. Z. Lu, G. Minhas, and J. Montesano, "The micro-damage process

zone during transverse cortical bone fracture: No ears at crack growth initiation," *J. Mech. Behav. Biomed. Mater.*, vol. 74, no. June, pp. 371–382, 2017.

[12] F. A. Sabet, A. R. Najafi, E. Hamed, and I. Jasiuk, "Modelling of bone fracture and strength at different length scales: A review," *Interface Focus*, vol. 6, no. 1, 2016.

[13] H. Peterlik, P. Roschger, K. Klaushofer, and P. Fratzl, "From brittle to ductile fracture of bone," *Nat. Mater.*, vol. 5, no. 1, pp. 52–55, 2006.

[14] T. San Antonio, M. Ciaccia, C. Müller-Karger, and E. Casanova, "Orientation of orthotropic material properties in a femur FE model: A method based on the principal stresses directions," *Med. Eng. Phys.*, 2012.

[15] L. L. Vignoli and P. P. Kenedi, "Bone anisotropy – Analytical and finite element analysis," *Lat. Am. J. Solids Struct.*, 2016.

[16] P. Zioupos, H. O. K. Kirchner, and H. Peterlik, "Ageing bone fractures: The case of a ductile to brittle transition that shifts with age," *Bone*, vol. 131, no. November 2019, p. 115176, 2020.

[17] R. Gauthier *et al.*, "Strain rate influence on human cortical bone toughness: A comparative study of four paired anatomical sites," *J. Mech. Behav. Biomed. Mater.*, vol. 71, no. March, pp. 223–230, 2017.

[18] Y. Li and S. M. Yu, "Targeting and mimicking collagens via triple helical peptide assembly," *Curr. Opin. Chem. Biol.*, vol. 17, no. 6, pp. 968–975, 2013.

[19] C. A. Miles and A. J. Bailey, "Thermal denaturation of collagen revisited," *Proc. Indian Acad. Sci. - Chem. Sci.*, vol. 111, no. 1, pp. 71–80, 1999.

[20] A. Gautieri, M. J. Buehler, and A. Redaelli, "Deformation rate controls elasticity and unfolding pathway of single tropocollagen molecules," *J. Mech. Behav. Biomed. Mater.*, vol. 2, no. 2, pp. 130–137, 2009.

[21] M. Unal, "Raman spectroscopic determination of bone matrix quantity and quality augments prediction of human cortical bone mechanical properties," *J. Biomech.*, vol. 119, p. 110342, 2021.

[22] M. Unal and O. Akkus, "Raman spectral classification of mineral- and collagen-bound water's associations to elastic and post-yield mechanical properties of cortical bone," *Bone*, vol. 81,

pp. 315–326, 2015.

[23] B. Burton, A. Gaspar, D. Josey, J. Tupy, M. D. Grynpas, and T. L. Willett, “Bone embrittlement and collagen modifications due to high-dose gamma-irradiation sterilization,” *Bone*, vol. 61, pp. 71–81, 2014.

[24] P. Zioupos, J. D. Currey, and A. J. Hamer, “The role of collagen in the declining mechanical properties of aging human cortical bone,” *J. Biomed. Mater. Res.*, vol. 45, no. 2, pp. 108–116, 1999.

[25] S. P. Veres, J. M. Harrison, and J. M. Lee, “Mechanically overloading collagen fibrils uncoils collagen molecules, placing them in a stable, denatured state,” *Matrix Biology*, vol. 33. pp. 54–59, 2014.

[26] T. L. Willett, R. S. Labow, and J. M. Lee, “Mechanical overload decreases the thermal stability of collagen in an in vitro tensile overload tendon model,” *J. Orthop. Res.*, vol. 26, no. 12, pp. 1605–1610, 2008.

[27] T. L. Willett, R. S. Labow, N. C. Avery, and J. M. Lee, “Increased proteolysis of collagen in an in vitro tensile overload tendon model,” *Ann. Biomed. Eng.*, vol. 35, no. 11, pp. 1961–1972, 2007.

[28] J. D. Black and B. J. Tadros, “Bone structure: from cortical to calcium,” *Orthop. Trauma*, vol. 34, no. 3, pp. 113–119, 2020.

[29] M. Conward and J. Samuel, “Machining characteristics of the haversian and plexiform components of bovine cortical bone,” *J. Mech. Behav. Biomed. Mater.*, vol. 60, pp. 525–534, 2016.

[30] S. F. Lipson and J. L. Katz, “The relationship between elastic properties and microstructure of bovine cortical bone,” *J. Biomech.*, vol. 17, no. 4, 1984.

[31] R. Almany Magal, N. Reznikov, R. Shahar, and S. Weiner, “Three-dimensional structure of minipig fibrolamellar bone: Adaptation to axial loading,” *J. Struct. Biol.*, vol. 186, no. 2, pp. 253–264, 2014.

[32] A. Mayya, A. Banerjee, and R. Rajesh, “Haversian microstructure in bovine femoral cortices : An adaptation for improved compressive strength,” *Mater. Sci. Eng. C*, vol. 59, pp. 454–463,

2016.

[33] J. Lawrence Katz, H. S. Yoon, S. Lipson, R. Maharidge, A. Meunier, and P. Christel, “The effects of remodeling on the elastic properties of bone,” *Calcif. Tissue Int.*, vol. 36, no. 1 Supplement, 1984.

[34] M. Martiniaková, B. Grosskopf, R. Omelka, M. Vondráková, and M. Bauerová, “Differences among species in compact bone tissue microstructure of mammalian skeleton: Use of a discriminant function analysis for species identification,” *J. Forensic Sci.*, vol. 51, no. 6, pp. 1235–1239, 2006.

[35] D. Vashishth, K. E. Tanner, and W. Bonfield, “Experimental validation of a microcracking-based toughening mechanism for cortical bone,” *J. Biomech.*, vol. 36, no. 1, pp. 121–124, 2003.

[36] P. Zioupos, U. Hansen, and J. D. Currey, “Microcracking damage and the fracture process in relation to strain rate in human cortical bone tensile failure,” *J. Biomech.*, vol. 41, no. 14, pp. 2932–2939, 2008.

[37] G. E. Fantner *et al.*, “Sacrificial bonds and hidden length dissipate energy as mineralized fibrils separate during bone fracture,” *Nat. Mater.*, vol. 4, no. 8, pp. 612–616, 2005.

[38] B. Zappone, P. J. Thurner, J. Adams, G. E. Fantner, and P. K. Hansma, “Effect of Ca2+ ions on the adhesion and mechanical properties of adsorbed layers of human osteopontin,” *Biophys. J.*, vol. 95, no. 6, pp. 2939–2950, 2008.

[39] Z. Wu, T. C. Ovaert, and G. L. Niebur, “Viscoelastic properties of human cortical bone tissue depend on gender and elastic modulus.,” *J. Orthop. Res. Off. Publ. Orthop. Res. Soc.*, vol. 30, no. 5, pp. 693–699, May 2012.

[40] J. D. Currey, K. Brear, and P. Zioupos, “Strain rate dependence of work of fracture tests on bone and similar tissues: Reflections on testing methods and mineral content effects,” *Bone*, vol. 128, no. November 2002, p. 115038, 2019.

[41] P. Zioupos and J. D. Currey, “Changes in the stiffness, strength, and toughness of human cortical bone with age,” *Bone*, vol. 22, no. 1, pp. 57–66, 1998.

[42] Z. Manilay, E. Novitskaya, E. Sadovnikov, and J. McKittrick, “A comparative study of young

and mature bovine cortical bone," *Acta Biomater.*, vol. 9, no. 2, pp. 5280–5288, 2013.

[43] T. L. Willett, D. Y. Dapaah, S. Uppuganti, M. Granke, and J. S. Nyman, "Bone collagen network integrity and transverse fracture toughness of human cortical bone," *Bone*, vol. 120, no. July 2018, pp. 187–193, 2019.

[44] R. Schneider, G. Faust, U. Hindenlang, and P. Helwig, "Inhomogeneous, orthotropic material model for the cortical structure of long bones modelled on the basis of clinical CT or density data," *Computer Methods in Applied Mechanics and Engineering*. 2009.

[45] S. Li, A. Abdel-Wahab, and V. V. Silberschmidt, "Analysis of fracture processes in cortical bone tissue," *Eng. Fract. Mech.*, vol. 110, pp. 448–458, 2013.

[46] S. Li, A. Abdel-Wahab, and V. V. Silberschmidt, "Analysis of fracture processes in cortical bone tissue," *Eng. Fract. Mech.*, vol. 110, pp. 448–458, 2013.

[47] P. Lucksanasombool, W. A. J. Higgs, R. J. E. D. Higgs, and M. V. Swain, "Fracture toughness of bovine bone: Influence of orientation and storage media," *Biomaterials*, vol. 22, no. 23, pp. 3127–3132, 2001.

[48] N. W. Smith, S. Ekwaro-Osire, M. Khandaker, and J. Hashemi, "Influence of Storage Duration on Retention of Original Fracture Toughness," *Exp. Mech.*, vol. 51, no. 5, pp. 697–705, 2011.

[49] L. Pruitt and A. Chakravartula, "Mechanics of Biomaterials: Fundamental Principles for Implant Design," *MRS Bull.*, vol. 37, Jul. 2012.

[50] J. Yan, J. J. Mecholsky, and K. B. Clifton, "How tough is bone? Application of elastic-plastic fracture mechanics to bone," *Bone*, vol. 40, no. 2, pp. 479–484, 2007.

[51] ASTM International, "ASTM C 1421 – 18 Standard Test Methods for Determination of Fracture Toughness of Advanced Ceramics at Ambient Temperature," *Am. Soc. Test. Mater.*, pp. 1–33, 2018.

[52] J. Yan, K. B. Clifton, J. J. Mecholsky, and R. L. Reep, "Fracture toughness of manatee rib and bovine femur using a chevron-notched beam test," *J. Biomech.*, vol. 39, no. 6, pp. 1066–1074, 2006.

[53] A. R. Boccaccini, R. D. Rawlings, and I. Dlouhý, "Reliability of the chevron-notch technique

for fracture toughness determination in glass," *Mater. Sci. Eng. A*, vol. 347, no. 1–2, pp. 102–108, 2003.

[54] D. Vashishth, J. C. Behiri, and W. Bonfield, "Crack growth resistance in cortical bone: Concept of microcrack toughening," *J. Biomech.*, vol. 30, no. 8, pp. 763–769, 1997.

[55] M. E. Launey, P. Y. Chen, J. McKittrick, and R. O. Ritchie, "Mechanistic aspects of the fracture toughness of elk antler bone," *Acta Biomater.*, vol. 6, no. 4, pp. 1505–1514, 2010.

[56] J. Yan, A. Daga, R. Kumar, and J. J. Mecholsky, "Fracture toughness and work of fracture of hydrated, dehydrated, and ashed bovine bone," *J. Biomech.*, vol. 41, no. 9, pp. 1929–1936, 2008.

[57] J. Hwang *et al.*, "Molecular assessment of collagen denaturation in decellularized tissues using a collagen hybridizing peptide," *Acta Biomater.*, vol. 53, pp. 268–278, 2017.

[58] J. L. Zitnay *et al.*, "Molecular level detection and localization of mechanical damage in collagen enabled by collagen hybridizing peptides," *Nat. Commun.*, vol. 8, 2017.

[59] M. I. Converse, R. G. Walther, J. T. Ingram, Y. Li, S. M. Yu, and K. L. Monson, "Detection and characterization of molecular-level collagen damage in overstretched cerebral arteries," *Acta Biomater.*, vol. 67, pp. 307–318, 2018.

[60] J. L. Zitnay *et al.*, "Accumulation of collagen molecular unfolding is the mechanism of cyclic fatigue damage and failure in collagenous tissues," *Sci. Adv.*, vol. 6, no. 35, 2020.

[61] L. Xiao *et al.*, "Molecular Detection and Assessment of Intervertebral Disc Degeneration via a Collagen Hybridizing Peptide," *ACS Biomater. Sci. Eng.*, vol. 5, no. 4, pp. 1661–1667, 2019.

[62] H. Bonney, B. J. Colston, and A. M. Goodman, "Regional variation in the mechanical properties of cortical bone from the porcine femur," *Med. Eng. Phys.*, vol. 33, no. 4, pp. 513–520, 2011.

[63] B. M. Jenkins, "A simple Machining Jig for Chevron-Notched Specimens," *Trans. Japan Inst. Met.*, vol. 29, no. 7, pp. 570–572, 1988.

[64] J. S. Nyman, A. Roy, X. Shen, R. L. Acuna, J. H. Tyler, and X. Wang, "The influence of water removal on the strength and toughness of cortical bone," *J. Biomech.*, vol. 39, no. 5, pp. 931–938, 2006.

[65] C. H. Turner and D. B. Burr, “Basic biomechanical measurements of bone: A tutorial,” *Bone*, vol. 14, no. 4, pp. 595–608, 1993.

[66] N. Reznikov, R. Almany-Magal, R. Shahar, and S. Weiner, “Three-dimensional imaging of collagen fibril organization in rat circumferential lamellar bone using a dual beam electron microscope reveals ordered and disordered sub-lamellar structures,” *Bone*, vol. 52, no. 2, pp. 676–683, 2013.

[67] K. Tai, H. J. Qi, and C. Ortiz, “Effect of mineral content on the nanoindentation properties and nanoscale deformation mechanisms of bovine tibial cortical bone,” *J. Mater. Sci. Mater. Med.*, vol. 16, no. 10, pp. 947–959, 2005.

[68] Z. Mohammadi, S. Shalavi, and H. Jafarzadeh, “Ethylenediaminetetraacetic acid in endodontics,” *Eur. J. Dent.*, vol. 7, no. 5 SUPPL., 2013.

[69] E. Sales *et al.*, “Study of composition and structure of demineralized bone using X-ray techniques,” *Radiat. Phys. Chem.*, vol. 167, no. May 2019, p. 108310, 2020.

[70] S. Pang, F. Y. Su, A. Green, J. Salim, J. McKittrick, and I. Jasiuk, “Comparison of different protocols for demineralization of cortical bone,” *Sci. Rep.*, vol. 11, no. 1, pp. 1–10, 2021.

[71] I. Kiviranta, M. Tammi, R. Lappalainen, T. Kuusela, and H. J. Helminen, “The rate of calcium extraction during EDTA decalcification from thin bone slices as assessed with atomic absorption spectrophotometry,” *Histochemistry*, vol. 68, no. 2, pp. 119–127, 1980.

[72] 3Helix, “3Helix CHP- 3Helix_user_guide_2021.07.28.pdf,” 2021. [Online]. Available: https://www.3helix.com/wp-content/uploads/2021/07/3Helix_CHP_user_guide_2021.07.28.pdf. [Accessed: 21-Nov-2005].

[73] J. Hwang *et al.*, “In Situ Imaging of Tissue Remodeling with Collagen Hybridizing Peptides,” *ACS Nano*, vol. 11, no. 10, pp. 9825–9835, 2017.

[74] J. Schindelin *et al.*, “Fiji: An open-source platform for biological-image analysis,” *Nat. Methods*, vol. 9, no. 7, pp. 676–682, 2012.

[75] M. Granke, M. D. Does, and J. S. Nyman, “The Role of Water Compartments in the Material Properties of Cortical Bone,” *Calcif. Tissue Int.*, vol. 97, no. 3, pp. 292–307, 2015.

[76] L. Fauch *et al.*, “Narrowband-autofluorescence imaging for bone analysis,” *Biomed. Opt.*

Express, vol. 10, no. 5, p. 2367, 2019.

[77] A. I. Prentice, "Autofluorescence of bone tissues.," *J. Clin. Pathol.*, vol. 20, no. 5, pp. 717–719, 1967.

[78] M. Cutini, M. Corno, D. Costa, and P. Ugliengo, "How Does Collagen Adsorb on Hydroxyapatite? Insights from Ab Initio Simulations on a Polyproline Type II Model," *J. Phys. Chem. C*, vol. 123, no. 13, pp. 7540–7550, 2019.

[79] C. D. Flanagan, M. Unal, O. Akkus, and C. M. Rimnac, "Raman spectral markers of collagen denaturation and hydration in human cortical bone tissue are affected by radiation sterilization and high cycle fatigue damage," *J. Mech. Behav. Biomed. Mater.*, vol. 75, no. June, pp. 314–321, 2017.

[80] P. Zioupos, X. T. Wang, and J. D. Currey, "Experimental and theoretical quantification of the development of damage in fatigue tests of bone and antler," *J. Biomech.*, vol. 29, no. 8, pp. 989–1002, 1996.

[81] T. L. Willett, B. Burton, M. Woodside, Z. Wang, A. Gaspar, and T. Attia, "γ-Irradiation sterilized bone strengthened and toughened by ribose pre-treatment," *J. Mech. Behav. Biomed. Mater.*, vol. 44, pp. 147–155, 2015.

[82] R. T. Borlinghaus and Lieca, "Pinhole Effect in Confocal Microscopes," 2017. [Online]. Available: https://www.leica-microsystems.com/science-lab/pinhole-effect-in-confocal-microscopes/.

[83] A. León-López, A. Morales-Peñaloza, V. M. Martínez-Juárez, A. Vargas-Torres, D. I. Zeugolis, and G. Aguirre-Álvarez, "Hydrolyzed Collagen—Sources and Applications," *Molecules* , vol. 24, no. 22. 2019.

[84] A. H. Lin, J. L. Zitnay, Y. Li, S. M. Yu, and J. A. Weiss, "Microplate assay for denatured collagen using collagen hybridizing peptides," *J. Orthop. Res.*, vol. 37, no. 2, pp. 431–438, 2019.

[85] L. Song, E. J. Hennink, I. T. Young, and H. J. Tanke, "Photobleaching kinetics of fluorescein in quantitative fluorescence microscopy," *Biophys. J.*, vol. 68, no. 6, pp. 2588–2600, 1995.

[86] D. M. Black *et al.*, "An assessment tool for predicting fracture risk in postmenopausal

women," *Osteoporos. Int.*, vol. 12, no. 7, pp. 519–528, 2001.

[87] P. Ammann and R. Rizzoli, "Bone strength and its determinants.," *Osteoporos. Int.*, vol. 14 Suppl 3, pp. 13–18, 2003.

[88] M. Saito and K. Marumo, "Collagen cross-links as a determinant of bone quality: A possible explanation for bone fragility in aging, osteoporosis, and diabetes mellitus," *Osteoporos. Int.*, vol. 21, no. 2, pp. 195–214, 2010.

Appendix A

Supplementary Images

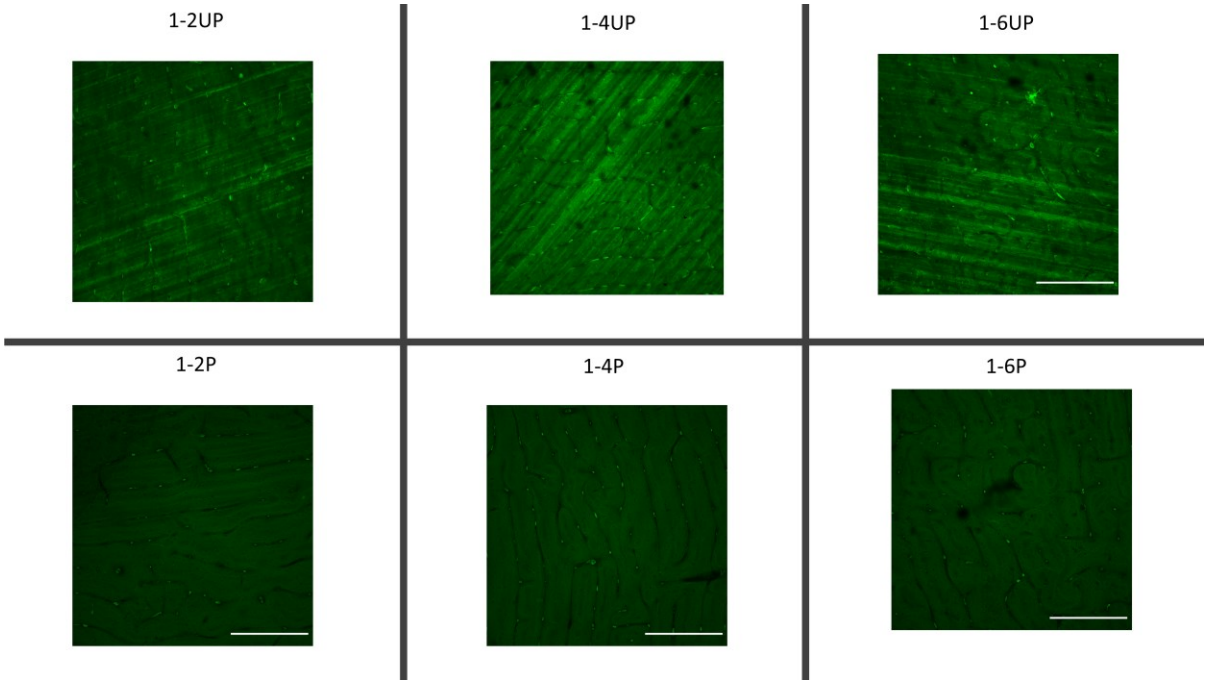

Figure A-1: Control images from hydrated samples from bone 2

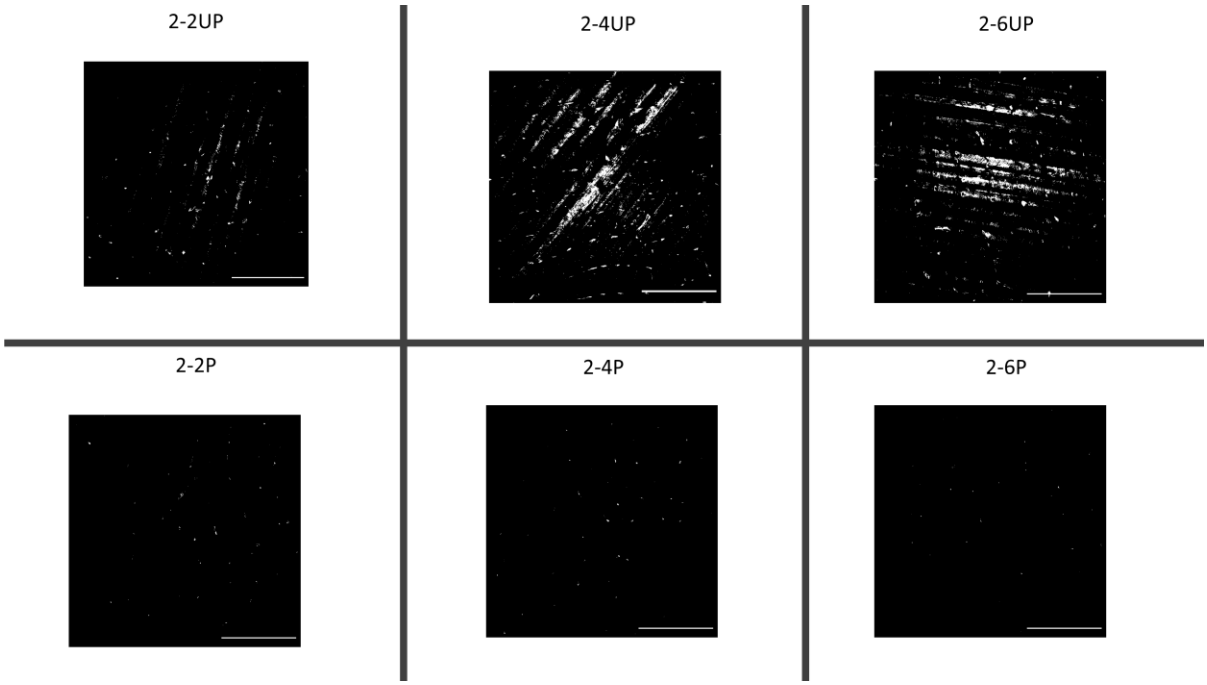

Figure A-2: Thresholded controls from hydrated experiment bone 2

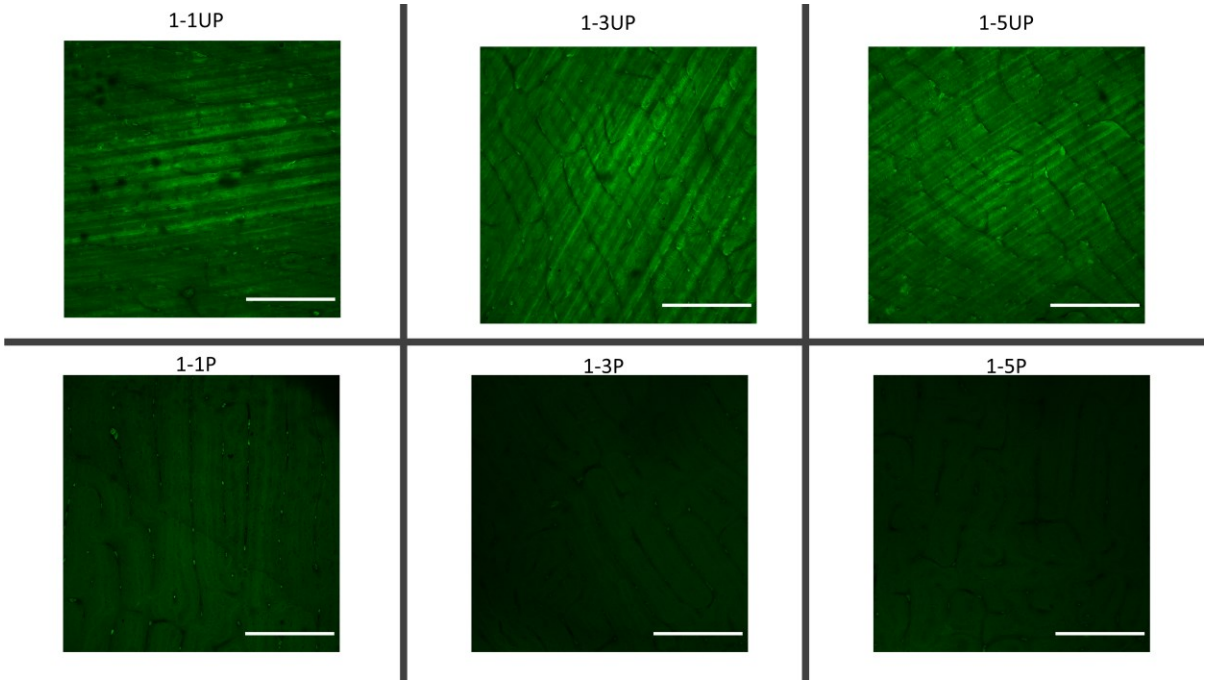

Figure A-3: Controls from bone 1 dehydrated experiment

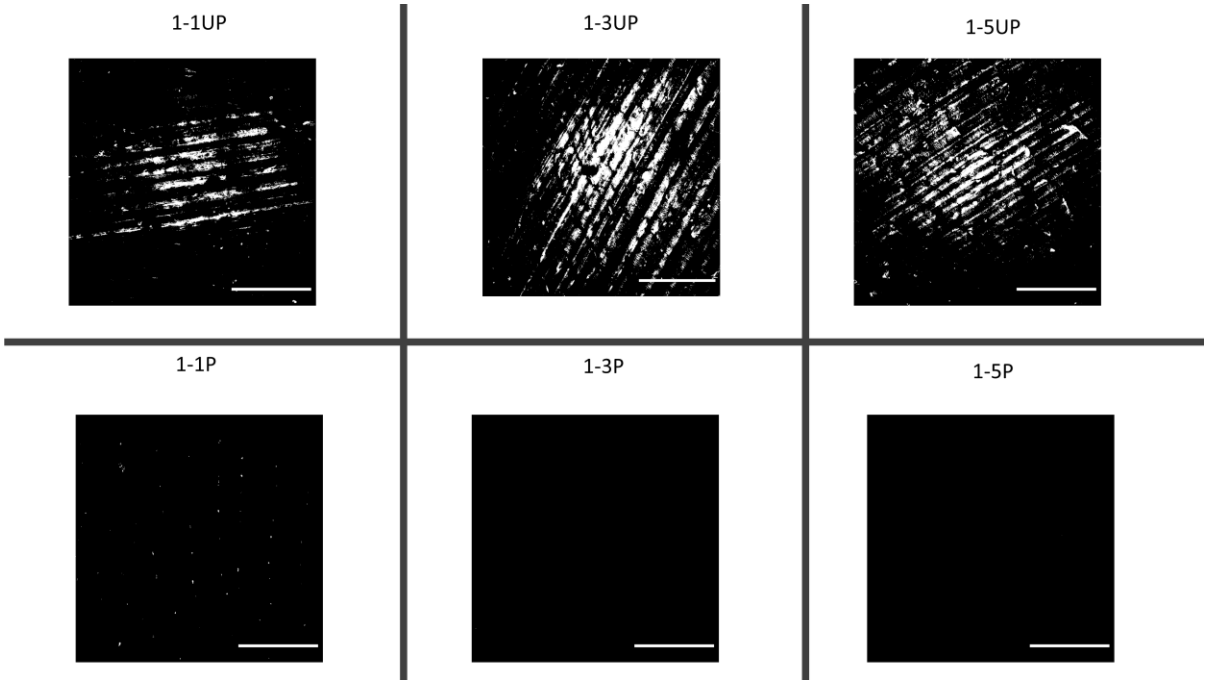

Figure A-4: Thresholded controls from bone 1 dehydrated experiment

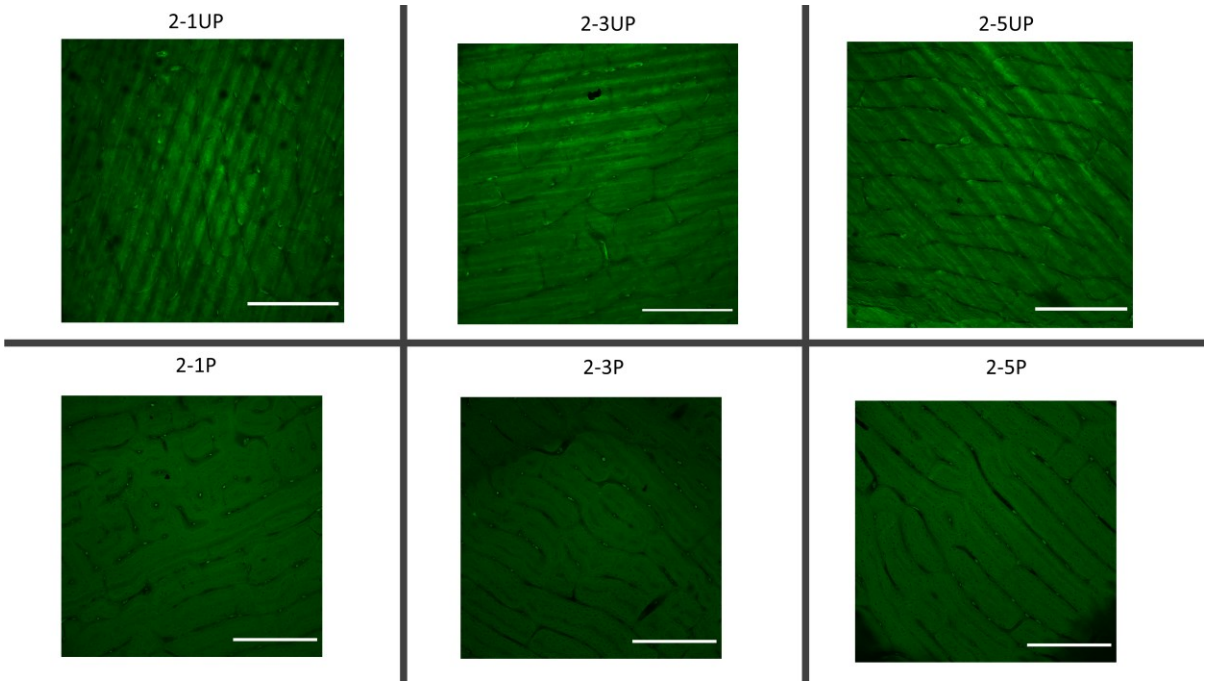

Figure A-5: Controls from bone 2 dehydrated experiment

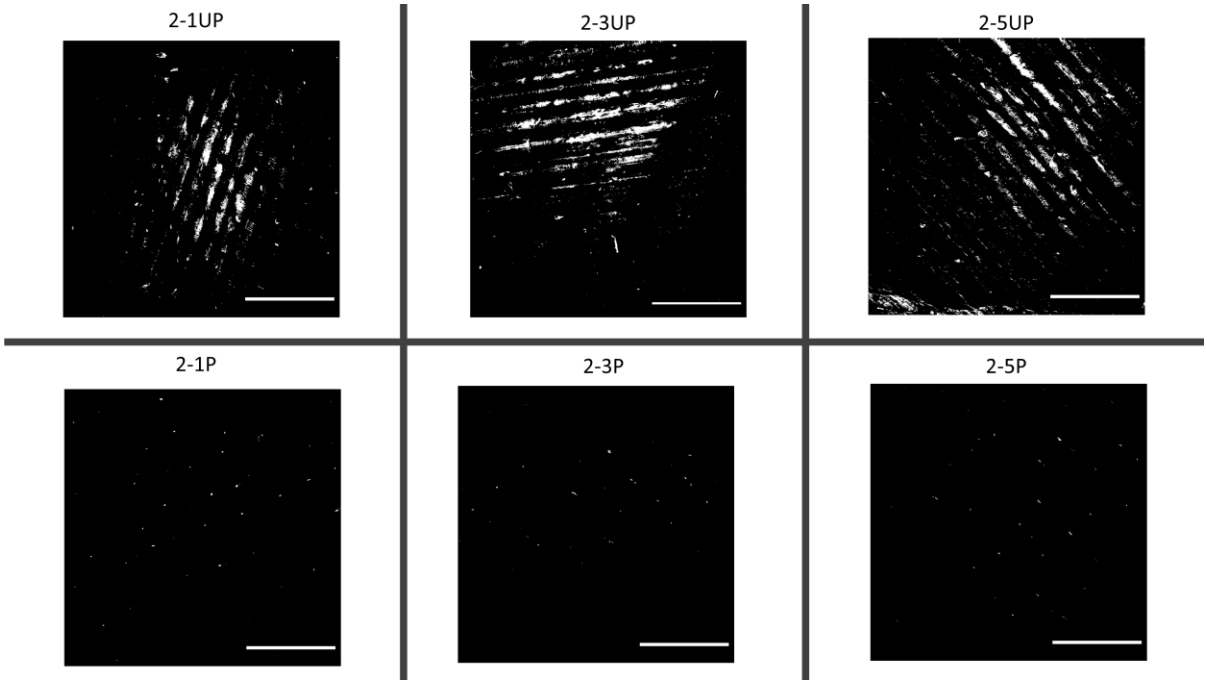

Figure A-6: Controls from the bone 2 dehydrated experiment

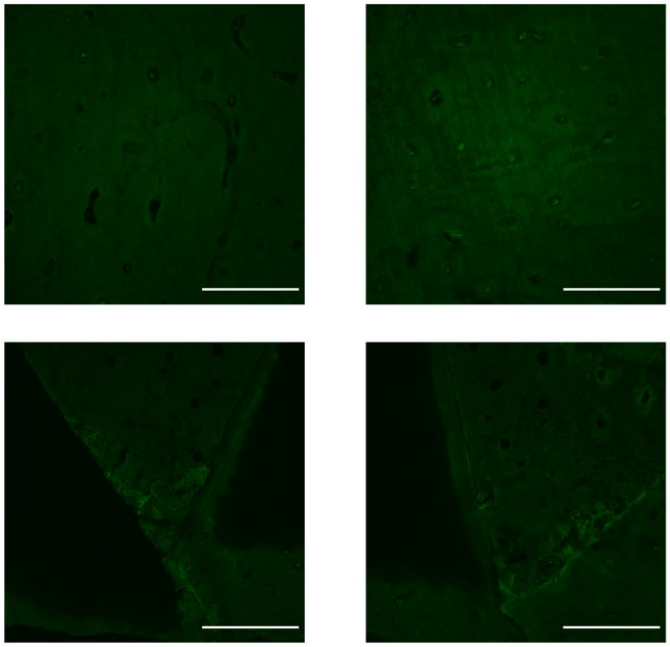

Figure A-7: F-CHP stained human bone, distal femur. No brightness adjustment. All scale bars 500 microns

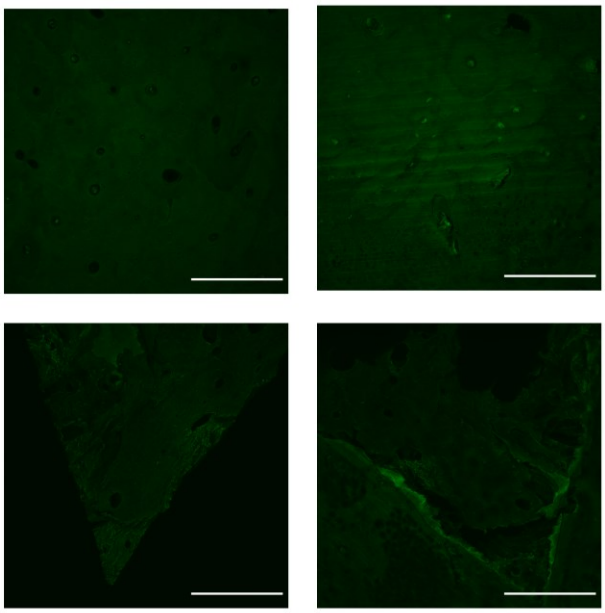

Figure A-8: F-CHP stained human bone, proximal femur, No brightness adjustment. All scale bars 500 microns

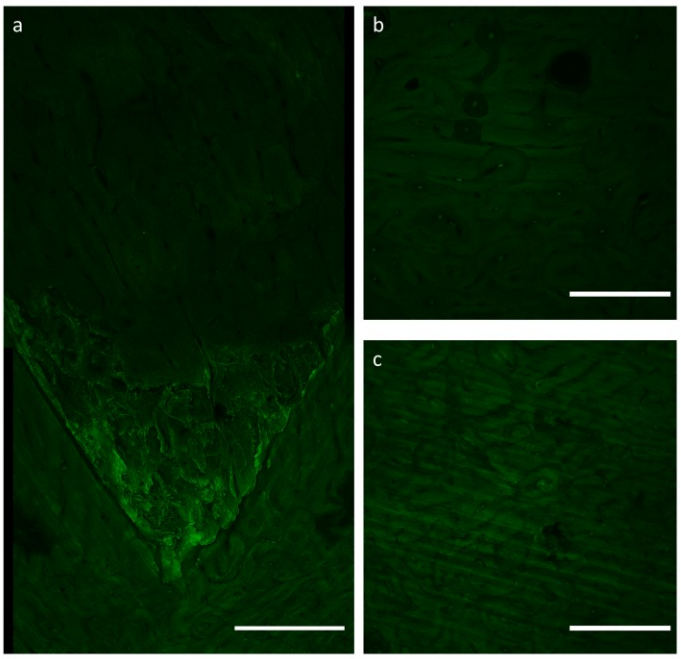

Figure A-9: a) Fracture surface compared to SEM imaging without brightness adjustment. b) Paired polished control without brightness adjustment. c) Paired unpolished control without brightness adjustment. All scale bars 500 microns.